Chiral Gd-DOTA as a Versatile Platform for Hepatobiliary and Tumor Targeting MRI Contrast Agents

Weiyuan Xu,[a,g‡] Xinjian Ye,[b‡] Min Wu,[c‡] Xin Jiang,[a] Lik Hang Hugo TSE,[d] Yanjuan Gu,[d*] Kun Shu,[c] Liuhui Xu,[e] Yong Jian,[a] Gengshen Mo,[a] Jiao Xu,[a] Yinghui Ding,[a] Ruonan Gao,[a] Jianliang Shen,[a] Fangfu Ye,[a,e,g*] Zhihan Yan,[b*] and Lixiong Dai[a,e,f*]

a. Wenzhou Institute, University of Chinese Academy of Sciences, Wenzhou, Zhejiang, 325000, China.
b. Department of Radiology, The Second Affiliated Hospital and Yuying Children's Hospital of Wenzhou Medical University, Wenzhou, Zhejiang, 325027, China.
c. Department of Radiology and Huaxi MR Research Center (HMRRC), Functional and Molecular Imaging Key Laboratory of Sichuan Province, West China Hospital, Sichuan University, Chengdu, Sichuan, 610041, China.
d. The Hong Kong Polytechnic University Shenzhen Research Institute, Shenzhen, Guangdong, 518057, China.
e. Joint Centre of Translational Medicine, The First Affiliated Hospital of Wenzhou Medical University, Wenzhou, Zhejiang, 325035, China.
f. Zhejiang Engineering Research Center for Innovation and Application of Intelligent Radiotherapy Technology, The Second Affiliated Hospital of Wenzhou Medical University, Wenzhou, Zhejiang, 325000, China
g. Oujiang Laboratory (Zhejiang Lab for Regenerative Medicine, Vision and Brain Health), Wenzhou, Zhejiang, 325000, China.

ABSTRACT: The leakage of gadolinium ion (Gd^{3+}) from commercial Gd^{3+}-based contrast agents (GBCAs) in patients is currently the major safety concern in clinical magnetic resonance imaging (MRI) scans, and the lack of task-specific GBCAs limits its usage in the early detection of disease and imaging of specific biological regions. Herein, ultra-stable GBCAs were constructed via decorating chiral Gd-DOTA with a phenylic analogue to one of the pendent arms, and the stability constant was determined as high as 27.08, accompanied with negligible decomplexation in 1 M of HCl over two years. A hepatic-specific chiral Gd-DOTA was screened out as a potential alternative to commercial Gd-EOB-DTPA, while combination with functional molecules favored chiral Gd-DOTA as tumor targeting probes. Therefore, the novel chiral Gd-DOTA is believed to be an ideal platform for designing next generation of GBCAs for various clinical purpose due to its outstanding inert nature.

INTRODUCTION

Gadolinium-based magnetic resonance imaging (MRI) contrast agents (CAs) have been used for more than 30 years clinically, and they are particularly useful to improve the soft-tissue contrast signal relative to non-contrast exams.[1] However, poor stabilities of many commercial GBCAs aroused increasing safety concerns over their clinical usage. Free Gd^{3+} released from GBCAs is very toxic because its ionic radius is very close to that of calcium ion (Ca^{2+}), which may result in the blockage of Ca^{2+} channels, thus affecting a series of physiological activities.[2] Since 2006, free Gd^{3+} are found to be associated with nephrogenic systemic fibrosis (NSF) in patients with renal impairment, leading to a contraindication of three least kinetically inert GBCAs (Gd-DTPA, Gd-DTPA-BMA and Gd-DTPA-BMEA) in certain patients by U.S. Food and Drug Administration (FDA) in 2010.[3-5] More recently, the long-term retention of Gd^{3+} in the brain has drawn great attention to the researchers, with studies found that more Gd^{3+} deposition was commonly associated with the administration of less inert GBCAs.[6, 7] As a consequence of currently strict regulatory status and safety risks of GBCAs, to develop GBCAs with enhanced stability would readily be the way out of the dilemma of commercial GBCAs.

Macrocyclic DOTA (1,4,7,10-tetraazacyclododecane-1,4,7,10-tetraacetic acid) is generally regarded as the "gold standard" for Gd^{3+} chelation, and Gd-DOTA is the most thermodynamically stable GBCA approved in clinical use.[8] Further improvements on its inertness could be achieved by introducing chiral groups to the macrocycle and pendant arms, in which steric effects prevent ring inversion and arm rotation, thus minimizing the interconversion among its stereoisomers.[9-11] According to the study of lanthanide NB-DOTA complexes, it is suggested that the steric hindrance induced from a single benzyl group to the macrocycle could hardly avoid the interconversion between its two pairs of isomers,[12] while the stereoisomers of chiral lanthanide DOTA complexes could be unprecedentedly stabilized via symmetrical decoration of four chiral groups to the backbone.[10] Besides, the steric hindrance induced by chiral groups prevents the interactions between the chelated metal ions and outer species, contributing to the kinetic inertness of complex as well. For example, the square antiprismatic (SAP) isomer of Gd-E4DOTA in Figure 1 exhibited no decomplexation after 20 days of incubation in 1 M of HCl.[10] Due the high inertness of chiral lanthanide DOTA complexes of this type, their stereoisomers could be purified and used as ideal candidates for optical and bioapplications in the area of circularly polarized lumines-

cence (CPL) due to their high luminescence dissymmetry factor (g_{lum}) and emission intensity.[13-15] The water exchange kinetics of chiral Gd-DOTA complexes were found to be very fast, regardless of the four substituents to macrocycle ranging in size from methyl to 4-aminobutyl, with water residence time (τ_M^{310K}) determined from 1.1 to 16 ns, which indicates ideal inner-sphere contribution as high field T_1 shortening MRI CAs.[10] Particularly, the longitudinal relaxivity (r_1) of Gd-E4DOTA was found to be higher than that of Gd-DOTA (4.2 (SAP), 3.9 (TSAP) *versus* 3.2 $mM^{-1}s^{-1}$), making it an ideal platform for CAs design.[10]

MRI technique requires micromolar levels of CAs to generate detectable signal enhancement, while most of the clinically approved GBCAs are nontargeted, thus demanding infusion of Gd^{3+} at gram level for patients in each MRI scan.[8] Yet, currently there are only two task-specific CAs for liver diagnostic applications, *i.e.* Gd-EOB-DTPA and Gd-BOPTA, but facing risks of Gd^{3+} leakage due to their poor inertness. Many mimics of Gd-EOB-DTPA have been reported by combining the lipophilic ethoxybenzyl (EOB) group with chelate skeletons including DO3A,[16, 17] PyC2A[18] and even nanoparticles.[19] Besides, difficulties aroused commonly in discrimination between normal tissue and lesions such as solid tumors, as common GBCAs have no significant difference in extravasation between them.[20] CAs targeting biomarkers for cancer specific MRI have been focused for decades, among which ZD2-N3-Gd(HP-DO3A) was reported as the first candidate reaching clinical trials approved by FDA in 2021.[21, 22] Small molecule GBCAs such as the linear Gd-DTPA or cyclic Gd-DOTA were widely adopted to bridge targeting molecules via amide bonds with their side arms but at the expense of inertness of complexes, which exacerbates the risk of their metal release.[23]

In our recent work, the inertness of Gd-DOTA was highly improved by introducing a phenylic group to one of its pendent arms,[24] while in this research, further improvements on its kinetic inertness and thermodynamic stability were achieved by decorating the macrocycle with extra chiral ethyl groups. The given chiral **Gd-L$_4$** (Figure 1) exhibited stability constant and pGd (pH 7.4) as high as 27.08 and 19.25 respectively. Then the developed both chiral and achiral Gd-DOTA complexes were screened in their *in vivo* biodistribution in mice via varying substitutions including nitro, carboxylic and methylsulfonyl groups to the *para*-site of the phenyl ring. One novel liver specific CA consisting four *R*-ethyl groups on the macrocycle and one *p*-nitrophenyl group on the pendent arm of Gd-DOTA (**Gd-L$_5$**, Figure 1) was constructed with comparable MRI performance to commercial Gd-EOB-DOTA, and its applicability in tumor diagnosis was verified using a mice model of orthotopic hepatocellular carcinoma (HCC). **Gd-L$_4$** bearing a carboxylic acid was further linked to small molecules including glucosamine and 3-nitrobenzene-sulfonamide analogues for MRI targeting solid tumor, in which **Gd-L$_8$** showed outstanding retention and penetration behavior towards the 4T1 solid tumor, thus deemed as an ideal candidate for developing hypoxic tumor targeting probes.

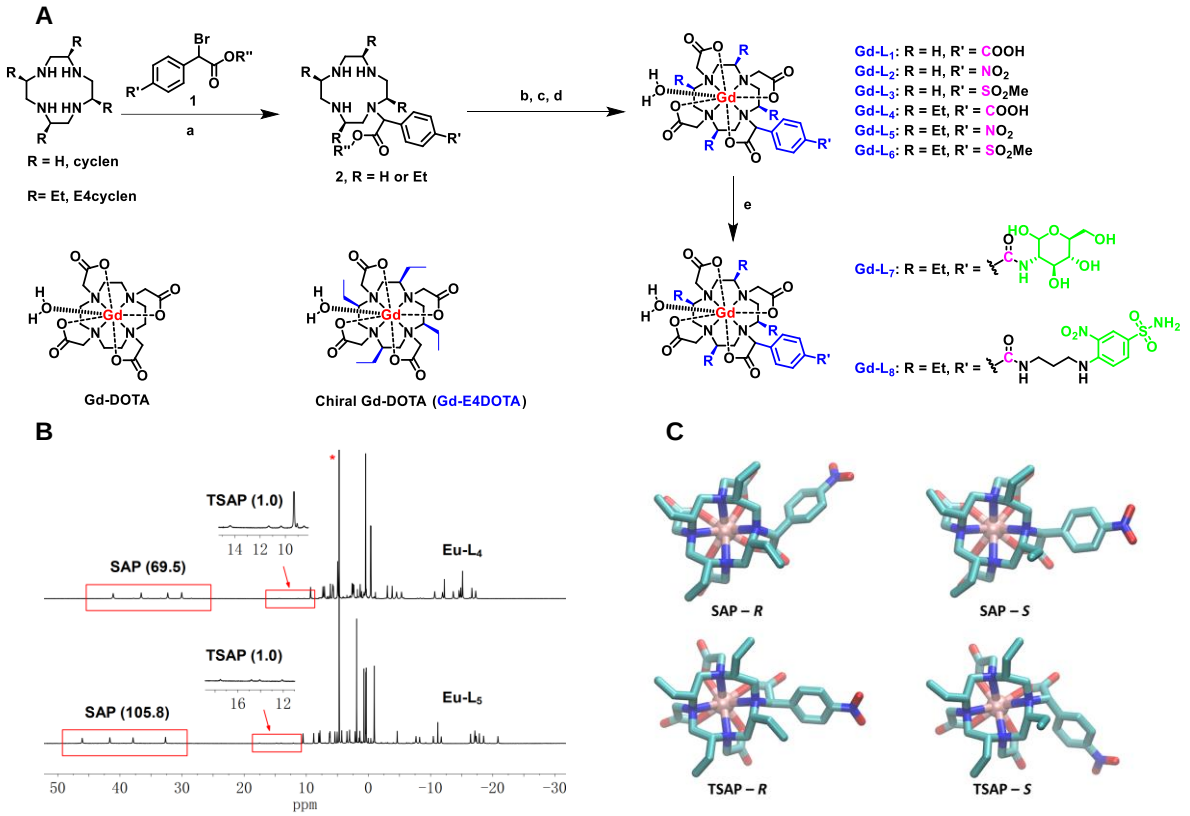

Figure 1. **Design strategy of Gd-DOTA analogues and the isomeric identification of chiral Gd-DOTA derivatives**. (**A**) Synthetic procedures. a) **1**, ACN, r.t.; b) K_2CO_3, ethyl bromoacetate, ACN, r.t.; c) LiOH, H_2O, MeOH, THF, r.t.; d) $GdCl_3{\cdot}6H_2O$, H_2O, reflux; e) glucosamine analogue or 3-nitrobenzene-sulfonamide analogue, EDCI, HoBt, DIPEA, DMF, r.t.. The counterions of complexes were omitted for clarity. (**B**) ^1H NMR spectra of **Eu-L$_4$** and **Eu-L$_5$** in D_2O. The characteristic peaks of SAP and twisted square antiprismatic (TSAP) isomers were grouped in red rectangles and both integrated with the integration of TSAP isomer set as 1.0. *indicates the residual peak of HDO. (**C**) Isomerization simulation of **Gd-L$_5$** by density functional theory (DFT). Atom labels: Gd (pink), C (green), N (blue) and O (red); H atoms were omitted for clarity.

Table 1. **Relaxivity and estimated log *P* of the investigated Gd^{3+} complexes**. Their r_1 and r_2 values were investigated in water and in the presence of 4.5% (w/v) HSA at 1.4 T and 37 °C. The relaxivity was presented as mean ± standard deviation (SD), n = 3.

Complexes	in water ($mM^{-1}s^{-1}$)		in 4.5% HSA ($mM^{-1}s^{-1}$)		log *P*
	r_1	r_2	r_1	r_2	
Gd-L_1	3.60±0.11	3.61±0.02	4.97±0.08	5.38±0.06	-1.71
Gd-L_2	4.00±0.08	4.24±0.06	5.97±0.07	6.52±0.19	0.65
Gd-L_3	4.19±0.02	4.24±0.05	4.70±0.08	4.88±0.12	0.20
Gd-L_4	4.89±0.09	4.99±0.07	7.35±0.15	10.13±0.60	0.85
Gd-L_5	5.13±0.01	5.59±0.11	7.51±0.06	9.80±0.25	1.40
Gd-L_6	5.25±0.03	5.61±0.04	6.47±0.05	6.57±0.23	1.20
Gd-L_7	6.79±0.02	6.92±0.07	7.48±0.10	8.50±0.18	0.95
Gd-L_8	5.31±0.04	5.44±0.08	10.13±0.10	18.74±0.27	1.43
Gd-DOTA	3.21±0.11	3.33±0.05	3.71±0.05	3.91±0.10	-2.87
Gd-EOB-DTPA	5.23±0.11	5.44±0.02	11.68±0.18	21.14±0.20	0.71

RESULTS AND DISCUSSION

Design and Synthesis of GBCAs. Structural modifications of DOTA have been widely investigated, with substitutions introduced to its macrocycle and pendant arms, where symmetric chiral substitutions on the macrocycle greatly improved the kinetic inertness of its lanthanide complexes.[11] In this research, both chiral and achiral Gd-DOTA analogues were constructed and evaluated for targeted diagnostics. Phenylacetate analogues were chosen as one of the pendant arms of the Gd-DOTA as shown in Figure 1A, as groups including methyl formate, nitro and methylsulfonyl moieties could be introduced to its *para*-site, thus modulating the properties of Gd-DOTA. Chiral cyclen (E4cyclen) in Figure 1A was synthesized according to the previous report with *R*-2-amino-1-butanol as the starting material.[10] As shown in Scheme S1 (supporting information, SI), bromination was firstly conducted at the α-carbon of phenylacetates in the presence of N-bromosuccinimide (NBS) and azodiisobutyronitrile (AIBN), and its products were further reacted with cyclen or E4cyclen via nucleophilic substitution (SN_2) at 1:1 ratio, with the rest of amines on macrocycles saturated with ethyl bromoacetate in next step. After hydrolysis in the presence of lithium hydroxide, the ligands were chelated with Gd^{3+} in neutral water, and the complexes **Gd-$L_{1\text{-}6}$** were finally purified with a semi-preparative reverse phase high performance liquid chromatography (RP-HPLC) system.

In order to identify the structural isomerism of chiral Gd-DOTA complexes, **L_4** and **L_5** were chelated with Europium (Eu^{3+}) for nuclear magnetic resonance (NMR) analysis. Both **Eu-L_4** and **Eu-L_5** were found to be nearly SAP pure as indicated by the four distinct peaks ranging from around 30 to 50 ppm in proton NMR spectra in Figure 1B. As the bromination has no chiral preference, compound **1** as the pendant arm contains both *R* and *S* isomers with the α-carbon as the chiral center, thus theoretically giving four stereoisomers for chiral **Gd-$L_{4\text{-}6}$**, while the stereoisomers induced by the *R* and *S* chirality could hardly be distinguished by NMR (Figure 1B). Similar stereoisomer preference was observed in previous study of DOTMA (bearing four *R*-methyl groups on arms), where TSAP geometry was found to be the privileged structure.[25] Considering the SAP/TSAP ratio of Eu-E4DOTA at 1/1.27,[10] it is suggested that the SAP preference of the chiral complexes in this research could be stabilized by the substitution of phenylic group to only one of the arms. The isomerism of **Gd-L_5** was further simulated in Figure 1C, which confirmed that the SAP isomer of chiral Gd-DOTA combined with the *S*-isomer of the phenylacetic arm (SAP-*S*) was capable of the lowest energy level, with relative higher energy states estimated at 4.66, 9.48 and 9.58 kJ/mol for SAP-*R*, TSAP-*S* and TSAP-*R* isomers respectively.

Rapid growth of tumor leads to dysfunctional microvasculature, generally featured with hypoxia, which protects tumors from therapy, thus with it emerging as an inevitable biomarker for consideration in developing tumor specific CAs.[26-28] For example, sulfonamides have been widely incorporated in CAs for targeting hypoxia *via* interacting with the carbonic anhydrase IX/XII overexpressed in hypoxic cancers.[29-31] Yet, the lack of selectivity among isoforms of human carbonic anhydrase usually brought unwanted side effects in their therapeutic applications.[32] 3-nitrobenzene-sulfonamide analogue exhibited better inhibition on tumor associated carbonic anhydrase IX/XII, and the reduction of nitro to amine group under hypoxic environment did not only improve the selectivity but also exerted enhanced cytotoxicity to tumor cells.[32, 33] The overexpression of various glucose transporters on cell membrane of cancers would be another ideal biomarker for targeting.[34] Then, **Gd-L_4** was conjugated to glucosamine and 3-nitrobenzene-sulfonamide analogue via a simple coupling reaction, giving **Gd-L_7** and **Gd-L_8** respectively. All the spectra for structural characterization including ^1H and ^{13}C NMR and mass spectrometry (MS) were given in supporting information (SI).

Relaxivity and log *P*. Longitudinal (r_1) and transverse (r_2) relaxivities of the investigated Gd^{3+} complexes were measured at 1.4 T and 37 °C to compare their efficiencies as contrast agents for MRI. Gd-DOTA in this research was found with r_1 and r_2 at 3.21 and 3.33 $mM^{-1}s^{-1}$ respectively in pure water, while with addition of an aromatic moiety to the α position of the pendant arm these values were enhanced slightly (3.60 to 4.24 $mM^{-1}s^{-1}$) as witnessed by **Gd-$L_{1\text{-}3}$** in Table 1. Both r_1 and r_2 were further improved by introduction of chiral groups (*R*-ethyl) to the macrocycle, with r_1 and r_2 ranging from 4.89 to 5.61 $mM^{-1}s^{-1}$ for **Gd-$L_{4\text{-}6}$**. The conjugation of **Gd-L_4** to 3-nitrobenzene-sulfonamide moiety led to an increase in r_1 from 4.89 to 5.31 $mM^{-1}s^{-1}$, while its linkage with glucosamine resulted in even higher relaxivities, *i.e.* 6.79 and 6.92 $mM^{-1}s^{-1}$ for r_1 and r_2 respectively.

The pharmacokinetics and biodistribution of CAs are known to be affected by extents of albumin binding, and generally strong binding with human serum albumin (HSA,

accounts for around 4.5% of plasma) prevents CAs from entering tissues such as hepatocyte, thus lowering the efficiency of blood clearance and tissue accumulation.[16] In this research, the binding of GBCAs with HSA was compared by evaluating their relaxivities in 4.5% HSA solution, where the tumble of CAs was slowed down upon binding macromolecule, thus generally resulting in enhancement in relaxivity.[35] Gd-DOTA in this research was found with slightly enhancement in r_1 after incubation with HSA, by 1.16 fold, and particularly **Gd-L$_2$** and **Gd-L$_5$** were proved with higher improvement in r_1, both by around 1.50 fold under the same condition, which assumes *p*-nitrophenylic moiety provides extra binding capacity with HSA. However, commercially hepatocyte specific Gd-EOB-DTPA provided the highest improvement in r_1 (by 2.23 folds) upon interacting with HSA, showing the highest affinity with HSA among the investigated CAs in this research due to the contribution of lipophilic *p*-ethoxybenzyl (EOB) group.

The albumin binding capacity of CAs is generally correlated with their lipophilicity, which indicates organ uptake (*e.g.* liver) and blood clearance of CAs could be estimated by assuming their partition coefficients (log *P*). In this research, a RP-HPLC method was referred for estimating the log *P* of GBCAs.[36, 37] As a very hydrophilic CA, Gd-DOTA was reported to be with a log *P* of -2.87,[38] and the log *P* of **Gd-L$_1$** was improved to be -1.71 because of the decoration of *p*-carboxyphenylic moiety. As the log *P* was associated with the hydrophilicity of decorated groups on the pendent arm, as shown in Table 1 it ascended in a sequence of *p*-carboxybenzene, *p*-methylsulfonylbenzene and *p*-nitrobenzene, and the chiral ethyl groups on macrocycle highly improved the log *P* as well, *e.g.* 0.65 and 1.40 for **Gd-L$_2$** and **Gd-L$_5$** respectively. The amphiphilic Gd-EOB-DTPA was tested with a log *P* value of 0.71 by using the same protocol.

Kinetic Inertness Assessments of GBCAs. The health risks of clinical GBCAs are associated with the release of Gd^{3+}, thus high inertness is required for developing safe GBCAs. The stability of GBCAs can be characterized by kinetic inertness and thermodynamic stability, in which kinetic inertness could be reflected by the rate of Gd^{3+} dissociation from the complexes while thermodynamic stability refers to the stability constant (log *K*) after reaching equilibrium of complexation.

Acid-assisted transmetallation is the main pathway to induce Gd^{3+} release of macrocyclic complexes, thus a relaxometric method was adopted in this research to compare the kinetic inertness of complexes in 1 M of HCl solution.[10, 11] As shown in Figure 2A, the change of transverse relaxation time (T_2) was given as the ratio to its original level, which exhibited decomplexation rate of the complexes along with incubation. Over 4 days of incubation at room temperature, **Gd-L$_{1\text{-}3}$** showed similar but slower rate of decomplexation compared to that of Gd-DOTA, which indicates that the adduct of a phenylic moiety at the α position of the acetate arm highly enhanced the kinetic inertness of Gd-DOTA analogues. The decomplexation of **Gd-L$_2$** in acid was further quantified using a RP-HPLC method, and as shown in Figure 2B, its half-lifetime ($t_{1/2}$) was expected to be 61 h, compared to that of Gd-DOTA at around 20 h.[39] Similarly, chiral **Gd-L$_{4\text{-}6}$** were analyzed by using both

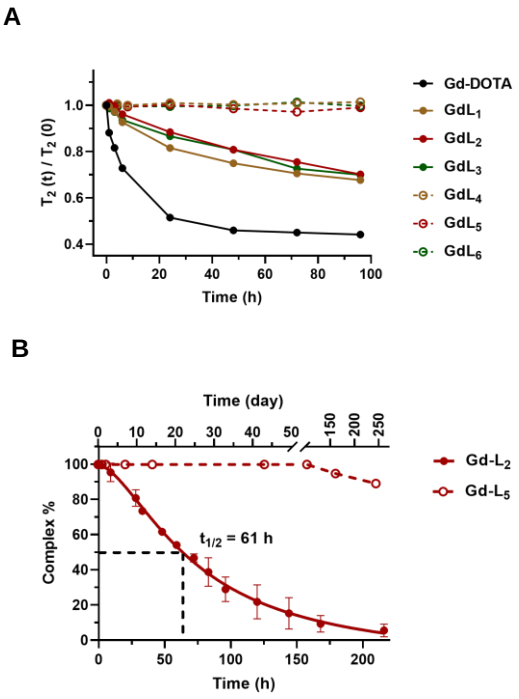

Figure 2. **Evaluation of inertness of GBCAs in 1 M of HCl solution at room tempeature**. T_2 relaxation time of CAs was recorded at 1.4 T, and inertness was compared via their deceasing rate of T_2 along with time (**A**); **Gd-L$_2$** and **Gd-L$_5$** were further analyzed through HPLC by fitting the area of absorption at 254 nm after certain time of incubation (**B**). Half-lifetime of **Gd-L$_2$** was acquired by performing a triplicate study.

relaxometric and HPLC methods. As shown in Figure 2A, obvious advantage in kinetic inertness was witnessed for chiral complexes **Gd-L$_{4\text{-}6}$** over their achiral counterparts **Gd-L$_{1\text{-}3}$** after 4 days of incubation in 1 M of HCl at room temperature as neglectable decomplexation was observed. Specially, **Gd-L$_5$** were observed with no degradation via HPLC analysis after up to 102 days of incubation in 1 M of HCl at room temperature, only with decomplexation determined at 5.2% and 10.8% after 161 and 244 days of incubation, respectively (Figure 2B and Figure S5). Surprisingly, **Gd-L$_4$** in 1 M of HCl was found with only 6.5% of decomplexation after 750 days of incubation at room temperature (Figure S5). Over half a year of incubation in 1 M of KOH at room temperature, the **Gd-L$_{1\text{-}6}$** showed neglectable release of metals and minimal transmetallation was observed for **Gd-L$_{1\text{-}6}$** in the presence of 10 folds of Zn^{2+} in phosphate buffered saline (PBS, pH 7.4) even after 6 days of incubation at 80 °C (Figure S4).

Thermodynamic Stability of GBCAs. In order to evaluate the thermodynamic stability, potentiometric titration was adopted in which protonation constants of ligands were determined firstly. The constant ionic background was maintained by dissolving ligands in 0.1 M of KCl solution, as potassium ion has much weaker interaction with ligands than sodium ion, thus minimizing the errors in the measurement.[40] Achiral **L$_{1\&2}$** and chiral **L$_{4\&5}$** were chosen for a comparison study. As shown in Table 2, each ligand was found with five protonation constants in this research in accordance with that of the parent ligand DOTA in the pre

Table 2. Protonation constants of ligands and stability constants of their complexes with Gd^{3+}.

	L_1	L_2	L_4	L_5	DOTA [a]
log K_{LH}	12.85±0.88	9.95±0.25	12.41±0.22	12.88±0.72	12.60
log K_{LH2}	9.18±0.20	9.90±0.38	11.19±0.20	10.10±0.12	9.70
log K_{LH3}	4.98±0.11	5.13±0.25	5.88±0.36	5.14±0.01	4.50
log K_{LH4}	3.61±0.18	4.33±0.47	4.73±0.22	4.88±0.01	4.14
log K_{LH5}	3.48±0.05	3.56±0.44	4.42±0.07	4.11±0.62	2.32
Σ log K_i^H	34.09±0.59	32.87±0.12	38.64±0.20	37.12±0.01	33.26
log K_{GdL}	25.39	25.49	27.08	26.80	24.7
pGd (pH 7.4) [b]	19.11	19.04	19.25	19.40	18.98

[a] Protonation constants taken from ref. 41; stability constant taken from ref. 42. [b] The pGd was defined as -log[free Gd] when [L] = 10 μM and [Gd] = 1 μM. The pGd of Gd-DOTA was acquired using the data in our previous report.[24]

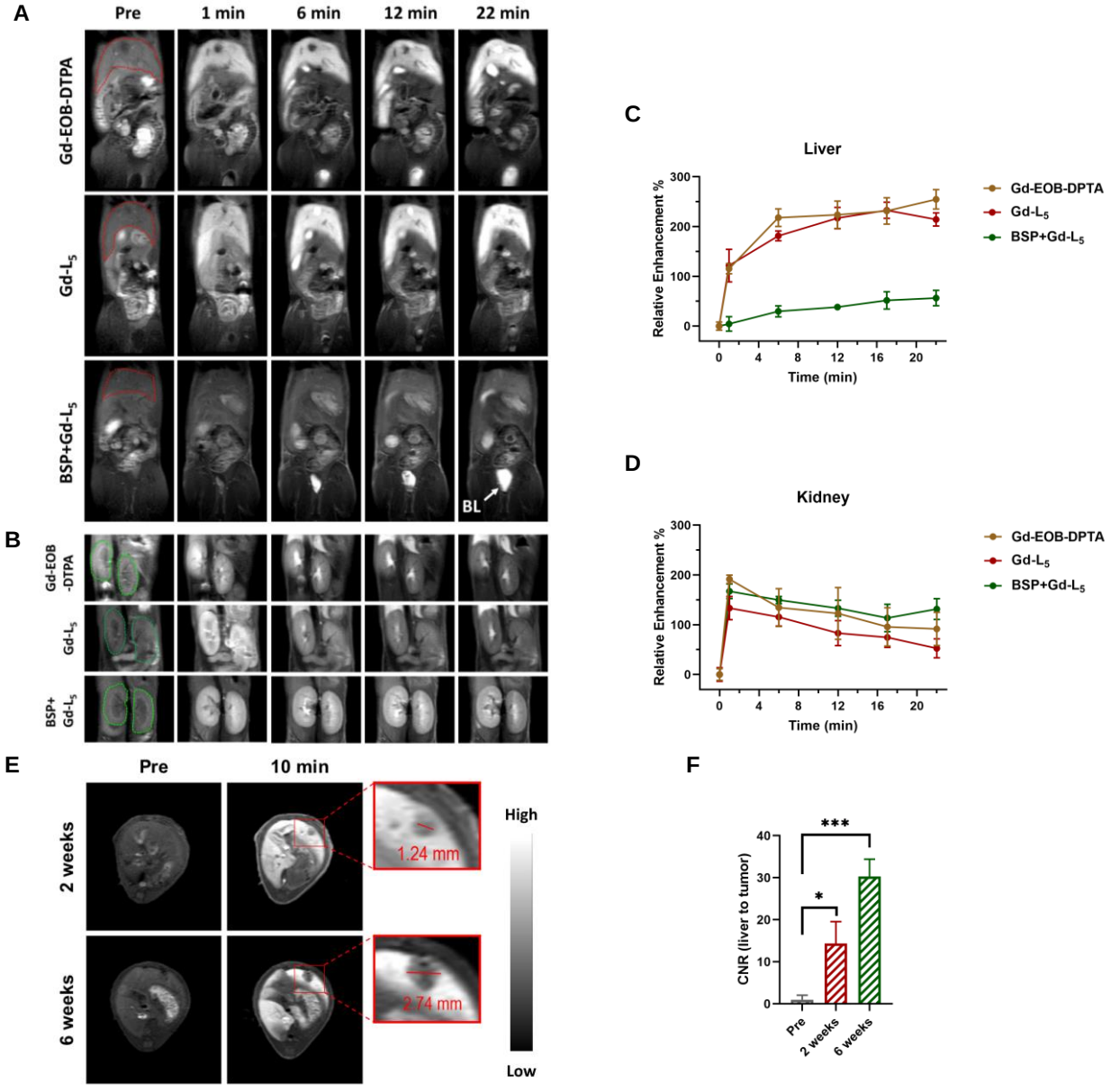

Figure 3. T_1-weighted *in vivo* liver targeting MRI and diagnosis of orthotopic HCC with the aid of Gd-L_5. The images of liver (**A**) and kidney (**B**) were captured prior and 1, 6, 12, 22 min post-injection of Gd-EOB-DTPA, **Gd-L_5** and BSP+**Gd-L_5** respectively, in which liver and kidney were outlined by the red and green dash lines respectively. BL, bladder. The signal changes of liver and kidney were expressed as relative enhancement to their initial signal intensity prior injection of CAs as shown in graph **C** and **D** respectively (n = 3). **E**. T_1-weighted MR images of liver implanted with orthotopic HCC before and after injection of **Gd-L_5**. **F**. Liver to tumor contrast to noise ratio (CNR) at 10 min post-injection of **Gd-L_5**. The mice were scanned 2 and 6 weeks after inoculation respectively. (n = 3, *P = 0.012, ***P < 0.001, unpaired t test).

vious report.[41] Although substituted with electron withdrawing groups to the α-position of one pendent arm, **L_1** and **L_2** showed similar basicity to that of DOTA, with total protonation constants determined at 34.09, 32.87 and 33.26 respectively. In contrast, **L_4** and **L_5** symmetrically bearing four *R*-ethyl groups on the macrocycle exhibited obviously higher total protonation constants (*i.e.* 38.64 and 37.12, respectively) than that of the parent ligand DOTA, where the first two protonation constants were associated to the protonation of the macrocycle,[43] but found relatively improved due to the electron donation of ethyl groups.

As the formation of Gd-DOTA analogues has extremely slow kinetics, an "out of cell" method was adopted to assess the thermodynamic stability of DOTA-type complexes, in which batch samples containing ligand and metal were prepared with variations in titrated potassium hydroxide.[43] As shown in Table 2, the stability constants of **Gd-$L_{1\&2}$** were found to be 25.39 and 25.49 respectively, which is slightly higher than that of Gd-DOTA (*i.e.* 24.7 [42]) in spite of their similar basicity. Chiral complexes **Gd-$L_{4\&5}$** exhibited even higher values at 27.08 and 26.80 respectively. Their pGd values at pH 7.4 were also compared, where the chiral **Gd-$L_{4\&5}$** were found with pGd at 19.25 and 19.40 respectively, which indicates obviously higher conditional stability than achiral **Gd-$L_{1\&2}$** (*i.e.* 19.11 and 19.04 respectively) and Gd-DOTA (18.98).

Hepatic *in vivo* MRI of mice. To develop task-specific GBCAs with improved safety profiles meets the demands of market and maximizes the advantage of MRI as a noninvasive technique. In the area of hepatobiliary MRI, currently there is no reliable alternative to commercial Gd-EOB-DTPA and Gd-BOPTA in spite of their instable characteristics. The complexes **Gd-$L_{1\text{-}6}$** were firstly investigated in normal mice for their biodistributions and pharmacokinetics, where a 3.0 T clinical scanner (Ingenia elition, Philips) was adopted for dynamic contrast enhanced MR scanning.

The coronal T_1-weighted images of **Gd-$L_{1\text{-}6}$** were listed in Figure 3A&B and Figure S8&S9, in which the excretion of complexes via liver and kidney was emphasized, and relative enhancement as a function of time was used to compare the degree of signal changes and prolonged retention of CAs in organs (Figure 3C&D and Figure S10). **Gd-L_5** was found with outstanding liver distribution while the other five complexes were witnessed with only renal excretion as shown in Figure 3A and Figure S8&S9. In order to evaluate the potential of **Gd-L_5** as the hepatocyte-specific CA, the commercial Gd-EOB-DTPA was adopted for comparison. Both **Gd-L_5** and Gd-EOB-DTPA reached the peak of contrast enhancement at around 20 min post-injection (Figure 3C) and obvious excretion into gallbladder was observed for both of them (Figure 3A). Upon administration of complexes, signal enhancement of kidney immediately peaked at 1 min post-injection for **Gd-L_5** and Gd-EOB-DTPA while this enhancement decreased gradually, accompanied with subsequent signal accumulation in urinary bladder (Figure 3B&D).

It is well known that the hepatic uptake of Gd-EOB-DTPA is transported by organic anion transporting polypeptides (OATPs), which plays a key role in pharmacokinetics of many drugs, and bromosulfophthalein (BSP) is able to bind OATPs strongly, thus inhibiting the transportation of Gd-EOB-DTPA.[37] Thus, BSP was adopted as the competitive inhibitor in this study to verify the mechanism behind hepatic uptake of **Gd-L_5**. Before administration of complex **Gd-L_5**, BSP was intravenously applied to mice and maintained at a level of 0.1 mmol/kg for 45 min, after which T_1-weighted images were recorded prior and post-injection of **Gd-L_5**. As shown in Figure 3A&C, minimal improvement of signal in liver was observed compared to the baseline. In contrast, its excretion via kidney was prolonged as evidenced by Figure 3B&D, which indicates the improved burden of kidney due to the loss of uptake by hepatocyte. Thus, OATPs transportation can be attributed as the pathway for hepatic uptake of **Gd-L_5**.

As the discrimination between healthy hepatocyte and tumor by contrast agents is attributed to the low OATPs expression in HCC,[19, 44] **Gd-L_5** was then used for detection of liver tumor. Human HuH7 tumor due to its limited OATPs expression was transplanted to the liver of mice in order to build orthotopic HCC model,[45] and the mice were further fed 2 and 6 weeks respectively after inoculation before MR scanning. Consecutive T_1-weighted scanning was applied for 26 min under a 3.0 T clinical magnet, and the hepatic lesion was barely seen before administration of **Gd-L_5**, compared to the significantly enhanced contrast between normal liver tissue and tumor post-injection (Figure 3E and Figure S11). For both 2 and 6 weeks groups, the liver to tumor CNR peaked at around 10 min, followed with a decay after 20 min post-injection (Figure S11). As shown in Figure 3E, by 10 min post-injection, the tumor was visually measured with a diameter of around 1.24 mm in the liver of 2 weeks group, and obvious grow in size was witnessed by 6 weeks after inoculation, with the diameter reached around 2.74 mm. The increase in size of tumor leaded to improved contrast between hepatocyte and tumor, where the liver to tumor CNR grew from 5.2 in the mouse of 2 weeks to 30.3 in the mouse of 6 weeks at 10 min post-injection (Figure 3F), but visually both showing clear contrast for tumor diagnosis. In summary, **Gd-L_5** provided rapid diagnosis of orthotopic liver tumor upon injection, and early tumor with diameter of around 1 mm could be clearly observed. The early detection of liver tumor less than 2 mm would highly improve the cure rate by surgical resection before tumor induced vascular invasion.[46]

Molecular Docking Studies. The isoforms of OATPS including OATP1B1, OATP1B3 and OATP2B1 and Na^+-dependent taurocholate transporting polypeptide (NTCP) play a vital role in facilitating drug uptakes by liver, in which OATP2B1 and NTCP are expressed at similar but lower levels.[47] The pathway for hepatic uptake of **Gd-L_5** was further investigated taking advantage of molecular docking studies with Gd-EOB-DTPA as the comparison, in which the crystal structure of OATP1B1, OATP1B3, OATP2B1 and NTCP were referred to previous reports.[16, 48] As the two most abundant transporters expressed in the liver, the representations of OATP1B1 and OATP1B3 accommodated with **Gd-L_5** and Gd-EOB-DTPA were shown in Figure 4. **Gd-L_5** was found to be less favored by OATP1B1, with the energy release determined at -19.76 kJ/mol in contrast to that of -25.66 kJ/mol for Gd-EOB-DTPA, while higher score was observed for Gd-EOB-DTPA in terms of binding OATP1B3 than that of **Gd-L_5**, *i.e.* -33.28 and -26.29

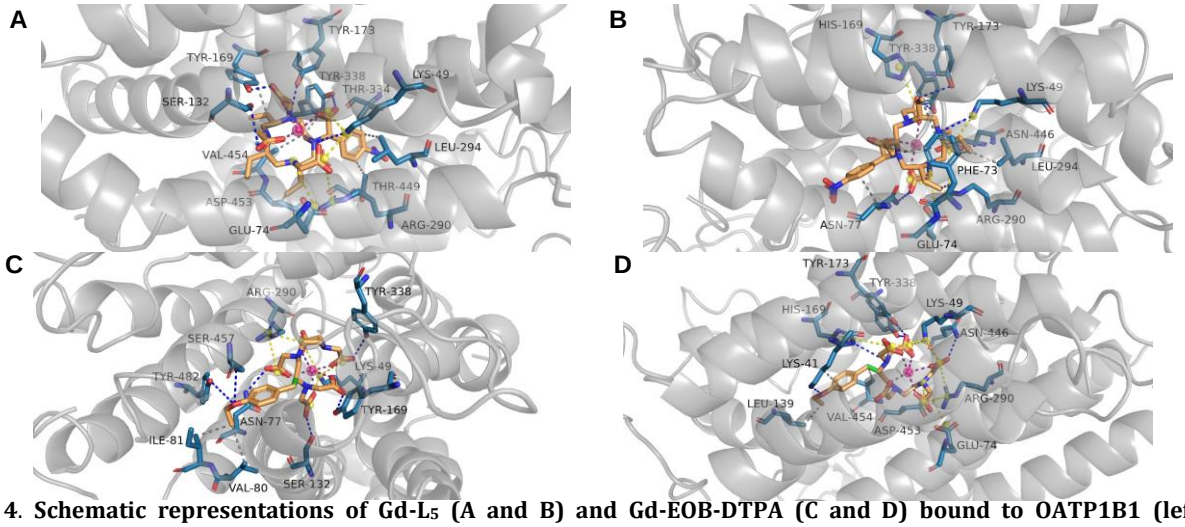

Figure 4. **Schematic representations of Gd-L$_5$ (A and B) and Gd-EOB-DTPA (C and D) bound to OATP1B1 (left) and OATP1B3 (right) respectively**. PDB code for OATPs, 2GFP. The hydrophobic interaction, hydrogen bond and salt bridge between GBCAs and transporters were indicated by gray, blue and yellow dash lines respectively.

kJ/mol respectively (Table S1). According to Figure 4 and Figure S12, the investigated GBCAs interacted with transporters mainly through hydrophobic interactions, hydrogen bonds and salt bridges, and generally the rigid **Gd-L$_5$** was preferred to build more hydrophobic interactions via both lipophilic ethyl and aromatic groups, but accompanied with less flexibility for accommodation in the transporting cavity in contrast to Gd-EOB-DTPA. Another gap between **Gd-L$_5$** and Gd-EOB-DTPA was witnessed in binding NTCP (*i.e.* -12.22 and -37.71 kJ/mol), while the inhibition constant of Gd-EOB-DTPA for NTCP was estimated as low as 0.25 μM compared to that of **Gd-L$_5$** higher than 1 mM (Figure S12 and Table S1). **Gd-L$_5$** was estimated with the highest affinity towards OATP2B1 (-33.24 kJ/mol), and a similar value of -38.34 kJ/mol was calculated for Gd-EOB-DTPA.

Biodistribution. In aforementioned *in vivo* MRI study, **Gd-L$_5$** was found to be an ideal candidate for liver targeting visualization, and clear discrimination between normal hepatic cells and HCC was demonstrated as well. A comparison of biodistribution between **Gd-L$_2$** and **Gd-L$_5$** was performed by analyzing the Gd^{3+} levels in brain, heart, liver, lung, spleen, intestine, muscle and kidney of mice post-injection respectively. As can be seen from Figure 5 and Table S2, dominated renal accumulation was observed for **Gd-L$_2$** at 5 min as high as 87.8 μg Gd^{3+} per g tissue, which was in accordance with the results from *in vivo* MRI (Figure S9). Neglectable retention of **Gd-L$_2$** in major organs was detected after 24 hours due to its rapid renal evacuation. In contrast, **Gd-L$_5$** was determined with 39.7 and 29.2 μg Gd^{3+} per g tissue at 5 min in liver and kidney respectively, and these two values went down rapidly along with time while an increase of Gd^{3+} in intestine was observed from 5 min to 30 min, due to the excretion of **Gd-L$_5$** from gallbladder (Figure 3A). The renal and hepatobiliary retentions of **Gd-L$_2$** and **Gd-L$_5$** were compared in Gd^{3+} percentage of total injection as shown in Figure 5 and Table S3. At 5 min post-injection, around 7% and 17% of **Gd-L$_2$** was detected in liver and kidney respectively in contrast to 28% and 6% of **Gd-L$_5$** in liver and kidney respectively. The hepatocyte uptake of **Gd-L$_5$** is only around half the amount of Gd-EOB-DTPA (around 50%),[24, 49] and this phenomenon is consistent with the lower affinities of **Gd-L$_5$** to trans-

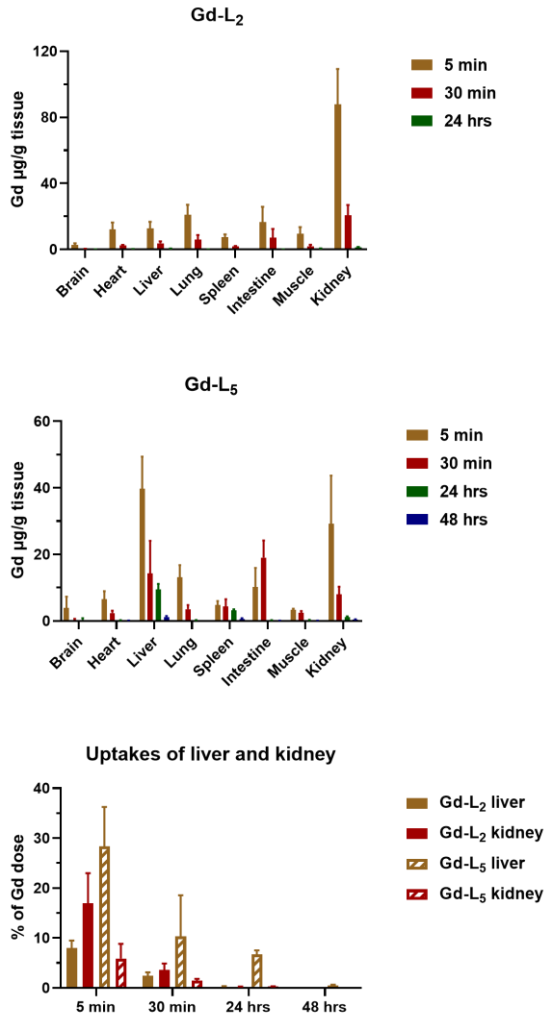

Figure 5. **Biodistribution of Gd-L$_2$ and Gd-L$_5$ in normal mice**. The Gd^{3+} contents were presented by μg per g tissue. The total uptakes of **Gd-L$_2$** and **Gd-L$_5$** were also compared as percentage of the injected dose. The results were given as mean ± SD, n = 3.

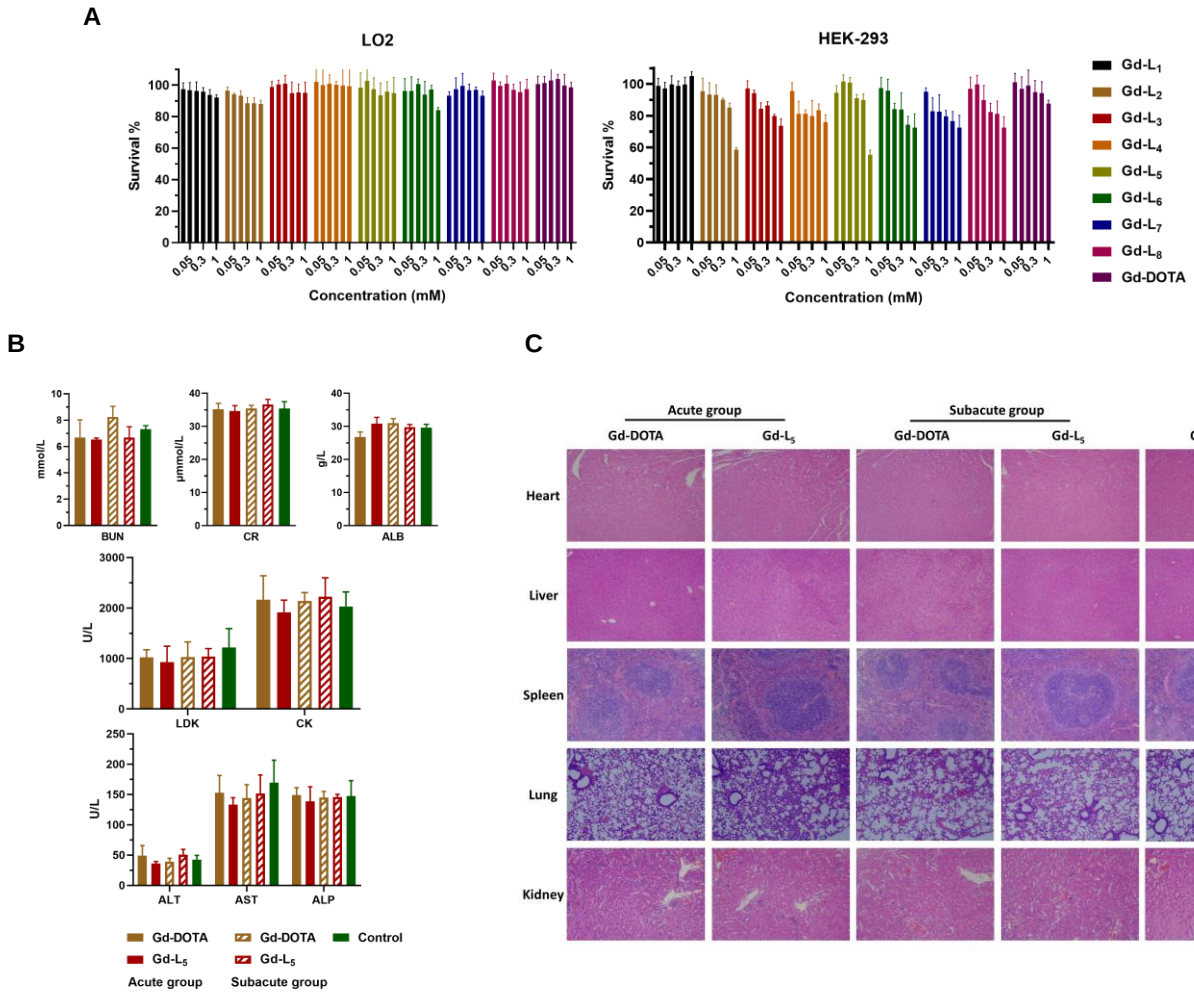

Figure 6. **Cytotoxicity and *in vivo* toxicity assessments**. (**A**) Cytotoxicity of **Gd-L$_{1\text{-}8}$** was evaluated in LO2 and HEK-293 cells respectively via a CCK-8 assay after incubation with 0.01, 0.05, 0.1, 0.3, 0.5 and 1.0 mM of complexes at 37 °C for 24 hours. Each value represents as the mean ± SD (n = 3). (**B**) Blood biomarkers including BUN, CR, ALB and various enzymes (ALT, AST, ALP, LDH and CK) were quantified for evaluation of acute and subacute toxicity towards mice after Gd-DOTA and **Gd-L$_5$** treatments. Each value represents as the mean ± SD (n = 3). (**C**) H&E staining histological analysis of major organs including heart, liver, spleen, lung and kidney. The acute and the subacute toxicity group of Gd-DOTA and **Gd-L$_5$** were compared with the control group.

porters including OATP1B1 and OATP1B3 as indicated in molecular docking study. The evacuation of **Gd-L$_5$** from liver took around two days, with about 7% and 0.5% of **Gd-L$_5$** detected in hepatic tissue at 24 and 48 hours post-injection respectively.

Toxicity Evaluation. The cytotoxicity of the investigated complexes **Gd-L$_{1\text{-}8}$** was examined in human fetal hepatocyte (LO2) and human embryonic kidney cells 293 (HEK-293) respectively. As shown in Figure 6A, the level of CAs was investigated as high as 1.0 mM for both cell lines, and all the CAs were found to induce neglectable toxicity towards LO2 cells while a dose dependent inhibition on HEK-293 cells was witnessed for GBCAs except **Gd-L$_1$**. At a concentration as high as 1 mM, the investigated GBCAs except **Gd-L$_{2\&5}$** exerted limited toxicity to HEK-293 cells, with viability found higher than 70%, while obvious inhibition was observed for both **Gd-L$_{2\&5}$**, with cell viability found less than 60%. Considering the fast clearance of GBCAs from the kidney, it is suggested that **Gd-L$_{1\text{-}8}$** would induce limited toxicity despite HEK-293 cells are more vulnerable than LO2 towards the investigated GBCAs of high concentrations.

As a potential candidate for clinical liver MRI, the acute and subacute toxicities of **Gd-L$_5$** were further examined in normal mice in comparison to commercial Gd-DOTA, in which mice of acute toxicity group were treated with 0.1 mmol/kg complexes one day before analysis while mice of subacute group were injected with same dose of complexes every one weeks for total 4 weeks. The control group was treated with PBS. The potential damage of complexes to the function of major organs were assessed by evaluating the biochemical parameters in blood. The levels of aspartate aminotransferase (AST), alanine aminotransferase (ALT), alkaline phosphatase (ALP) and albumin (ALB) were related to the function of liver while renal function could be reflected by concentrations of blood urea nitrogen (BUN) and creatinine (CR).[50] Activities of lactate dehydrogenase (LDH), creatinine kinase (CK) were also included in the analyses. Firstly, there was no obvious difference in the levels of BUN and CR for both GBCAs compared to the control group, which indicates the renal function was

not disrupted in both acute and subacute groups as shown in Figure 6B. In spite of slightly lower levels of CK and AST in acute group after administration of **Gd-L$_5$**, the other biomarkers in Figure 6B were found to be consistent to the levels of the control group, which demonstrates that Gd-DOTA and **Gd-L$_5$** have limited damage to liver and heart. Histological statuses of major organs including heart, liver, spleen, lung and kidney were shown in Figure 6C by using a hematoxylin and eosin (H&E) staining method, and neglectable abnormalities were observed in both acute and subacute toxicity groups after Gd-DOTA and **Gd-L$_5$** treatments. Particularly, clear and abundant glomerulus was found in images of kidney, and the hepatocytes was found with no inflammatory infiltrates. The lung and spleen were observed with neither fibrosis nor hyperplasia as well. All these results demonstrate the good *in vivo* safety profiles of Gd-DOTA and **Gd-L$_5$**, and particularly **Gd-L$_5$** is expected to be a potential candidate for hepatobiliary MRI in clinical trials.

***In vivo* MRI of Subcutaneous Tumor Mice**. Currently, none of the clinical GBCAs could be used for tumor-specific diagnosis, as tumor specific MRI requires higher accumulation of CAs than surrounding tissues. With the extremely stable **Gd-L$_4$** in hand, small molecules including glucosamine and 3-nitrobenzene-sulfonamide were easily conjugated to give **Gd-L$_7$** and **Gd-L$_8$** respectively for targeting tumor microenvironments, *i.e.* Warburg effect,[34, 51] and hypoxia.[28] As 4T1 tumor is a quickly growing, more aggressive malignancy with early central necrosis formation,[52] a subcutaneous tumor model was prepared by injecting 4T1 cells to the right side of mice axillary to mimic the hypoxia microenvironment. Then **Gd-L$_4$**, **Gd-L$_7$** and **Gd-L$_8$** were applied to the mice intravenously in order to compare their *in vivo* tumor targeting properties. Both coronal and axial MR images of tumor before and post-injection were shown in Figure 7, and all three investigated GBCAs provided clear borderlines between solid tumor and normal tissue upon injection as shown by the post 5 min images due to the angiogenesis of tumor. The tumor uptake of **Gd-L$_4$** was not significant within 2 hours of screening. Interestingly, the tumor treated with **Gd-L$_7$** was observed with gradual uptake by measuring the tumor to muscle CNR, with peak reached at 20 min, and stepwise drop was indicated from 20 min onwards (Figure 7B&C). As the reduction of the nitro group on 3-nitrobenzene-sulfonamide analogue could enhance its affinity to tumor associated carbonic anhydrase IX,[33] the enzyme catalyzed reduction of **Gd-L$_8$** under hypoxia condition was confirmed by using a hypoxia chamber, in which the nitro group was reduced to be amine as evidenced by HPLC-MS analysis (Figure S13). Specially, a clear drop in CNR between tumor and muscle was observed immediately after injection of **Gd-L$_8$** and gradual accumulation of signal intensity was observed from outer into inner regions of tumor in up to 2 hours (Figure 7B&C), constantly providing clear discrimination between tumor and the neighboring normal tissue. Visually, the renal excretion of **Gd-L$_8$** was observed with abnormally high signal level in kidney of mice up to 2 hours post-injection (Figure 7A), which may be due to its inevitable interaction with the carbonic anhydrase II expressed in kidney. [33, 53]

CONCLUSIONS

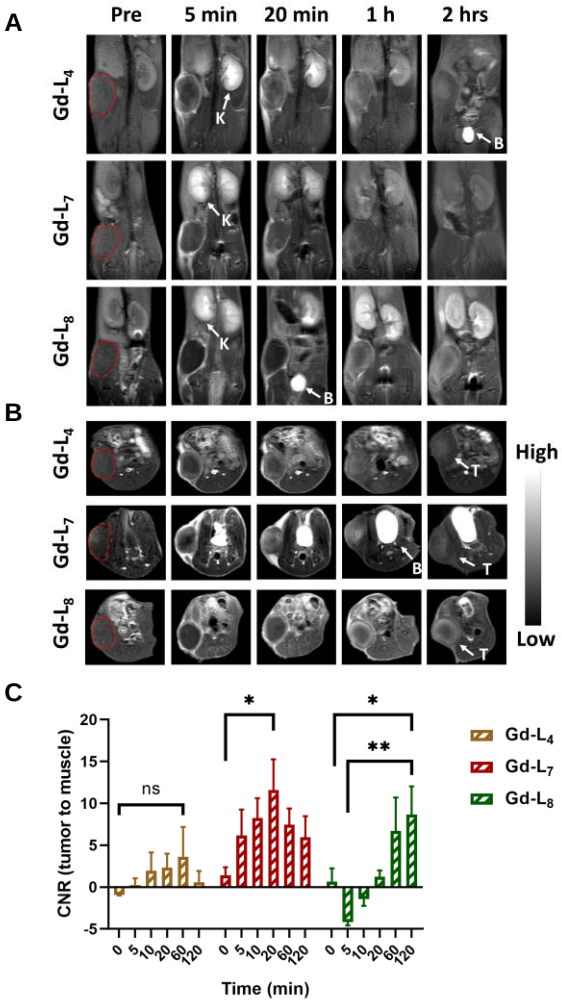

Figure 7. **The assessments of targeting GBCAs for MRI of 4T1 subcutaneous tumor**. **Gd-L$_4$**, **Gd-L$_7$** and **Gd-L$_8$** were injected to 4T1 bearing mice intravenously, and the coronal and axial T_1-weighted images are shown in (**A**) and (**B**) respectively. Tumors were outlined with red dash lines. K, kidney; T, tumor; B, bladder. (**C**) The tumor to muscle CNRs were compared over 2 hours post-injection. (n = 3, *P<0.03, **P<0.003; ns, not significant; unpaired t test).

A class of chiral Gd-DOTA complexes was developed through decorating chiral Gd-E4DOTA with a phenylic analogue to one of the arms, which exhibited unusual kinetic inertness, thus deemed as ideal candidates for developing safe GBCAs to avoid Gd^{3+} leakage in patients. A potential hepatobiliary GBCAs was screened out as **Gd-L$_5$** by decoration of a nitro group to the *para*-site of phenylic group, which exhibited comparable liver imaging quality to that of Gd-EOB-DTPA, clear discrimination of orthotopic HCC and minimal *in vivo* toxicity in mice, therefore deserving further investigations as an alternative to commercial Gd-EOB-DTPA under the guidelines of regulatory agency. The application of chiral Gd-DOTA in probing tumors was testified by introducing functional molecules to **Gd-L$_4$** via a simple coupling reaction, in which **Gd-L$_8$** bearing a 3-nitrobenzene-sulfonamide moiety showed prolonged retention in hypoxic tumor tissue, hopefully covering the lack of tumor specific GBCAs. Therefore, chiral Gd-DOTA is

emerging as a novel platform for designing next generation of GBCAs with high safety, and the introduction of task specific molecules to the agents is believed to a feasible strategy to meet the demands of clinical diagnosis of various scenarios.

MATERIALS AND METHODS

General Information. All chemicals and solvents for synthesis were acquired from commercial suppliers, including Energy (Shanghai, China), Macklin (Shanghai, China), Aladdin chemical (Shanghai, China) etc. and were used as received. Human serum albumin (HSA) was bought from Sigma-Aldrich (Beijing, China) as lyophilized powder, and it was dissolved in water as 22.5% (w/v) stocks and kept in 4 °C fridge before further usage. Gd-DOTA (Gadoteric acid, HENGRUI, Lianyungang, China) and Gd-EOB-DTPA (Gadoxetic acid, BAYER, Berlin, Germany) were acquired from clinics. The standard solution of HCl (1 M) and KOH (2 M) were supplied by BOLINDA technology CO. LTD. (Shenzhen, China). Deuterated solvents such as $CDCl_3$, D_2O and DMSO-d_6 were purchased from Macklin Chemical (Shanghai, China). All the nuclear magnetic resonance (NMR) spectra were performed on a 400/100 MHz spectrometer (Q.One Instruments, Wuhan, China). Liquid chromatography-mass spectrometry (LC-MS) was conducted on an Agilent ultraperformance liquid chromatography (UPLC) equipped with an electro spray ionization (ESI)-MS detector (1290 Infinity II + 6135MS), while the high resolution MS of Gd^{3+} complexes were recorded by using a Thermo Scientific Q Exactive Quadrupole-Orbitrap mass spectrometer. The purity of **Gd-L$_{1-8}$** was determined using reverse phase high performance liquid chromatography (RP-HPLC), and the purity of each complex was confirmed to be higher than 95%.

HPLC Methods. A Waters alliance e2695 RP-HPLC system equipped with a Waters C18 column (5 μm, 4.6 × 150 mm) was adopted for analytical study. The general analytical methods can be described as following: the pump started with 90% water containing 0.05% trifluoroacetic acid (TFA) (phase A) / 10% pure acetonitrile (phase B) at a constant flow rate of 1 mL/min, and then the percentage of B increased linearly to 100% in 10 min, with both A and B phases recovered to their initial contents in next 2 min and rinsed for another 3 min before next injection. A Waters semi-preparative RP-HPLC system equipped with a Waters C18 column (5 μm, 19 × 250 mm) was used for purification of ligands and their Gd^{3+} complexes, and similarly the instrument method started with 90% A and 10% B at a constant flow rate of 7 mL/min. In the following 20 min, both A and B phases were linearly changed to 50%, and before next injection the column was rinsed with 90% A and 10% B for 2 min. Photodiode array detectors were equipped for both analytical and semi-preparative HPLC systems.

DFT Calculations. All calculations were performed on the basis of PBE0/BSI level of theory by Gaussian 09 (revision D.01) software package.[54] The PBE0 functional has been proved suitable for lanthanides.[55] The BSI denotes a mixed basis set, which uses 6-311G(d) basis set for non-metal elements, m06 functional and MWB53 basis set for Gd^{3+}. Geometry optimizations were performed via the Berny algorithm until the total energy converged to within 1×10^{-6} Ha, the forces on all atoms were less than 0.0025 a.u., the maximum step size was less than 0.01 a.u., and the root mean square (RMS) force was less than 0.006 a.u.. The visualized molecular orbitals were shown as an iso-surface value of 0.02 a.u.. Water (H2O) was chosen as the solvent and the polarizable continuum model (PCM) was used as the solvent model. The relative conformation energy that indicates the coordination stability took the energy-minimal Gd^{3+} complex as the reference (0 kJ/mol).

Quantification of Gd^{3+}. The contents of Gd^{3+} in this research were quantified using an Agilent 7850 inductively coupled plasma mass spectrometry (ICP-MS). The samples for test were dissolved in 2% nitric acid and filtered using a 0.22 μm membrane before injection. The Gd^{3+} standards were diluted from the stock (1000 ppm, Guobiao Testing & Certification Co., Ltd., Beijing, China) to levels including 50, 100, 200, 300, 500 and 800 ppb with 2% nitric acid, and a standard curve for calibration was built by infusing Gd^{3+} standards in each measurement, with 1 ppb of Tb^{3+} as the inner standard simultaneously.

Relaxivity Measurements. The complexes **Gd-L$_{1-8}$** were dissolved in pure water (MilliQ, 18.2 MΩ·cm^{-1}) to levels of Gd^{3+} at 0.1, 0.2, 0.3, 0.4 and 0.5 mM respectively. The longitudinal (T_1) and transverse (T_2) retention time of samples (200 μL in NMR tube) were recorded on a 1.4 T MR magnet at 37 °C (60 MHz, Huan Tong Nuclear Magnetic, Shanghai, China), with the 90° and 180° pulse durations set at 37 and 75 μs respectively. For T_1 measurement the repetition time was set at 10.0 s with an inversion recovery experiment ranging from $0.05\times T_1$ to $5\times T_1$, while T_2 measurement included a CPMG pulse sequence, with the echo spacing and repetition time set at 3.0 ms and 5.0 s separately. The relaxivities r_1 and r_2 were determined by plotting $1/T_1$ or $1/T_2$ *versus* concentrations, which gave the slope of the linear fitting curve as the relaxivity. Then each tube was added with 50 μL of HSA stock (22.5%) and their T_1 and T_2 values were recorded subsequently under the same conditions. All the relaxivity measurements were performed in triplicates.

Log *P* Estimation. A previously reported RP-HPLC method was adopted for the estimation of log *P*.[36, 37] A RP-HPLC equipped with a Waters C18 column (5 μm, 4.6 × 150 mm) was adopted for sample analysis, and 20 mM ammonium acetate solution and pure acetonitrile were selected as mobile phase A and B respectively. Initially, 95% A and 5% B were eluted for 1 min at a flow rate of 1 mL/min, and the content of B increased to 50% from 1 to 10 min, then to 95% in 1 min. The content of B remained unchanged at 95% for 1 min while this content dropped to 5% from 12 to 13 min, with the column rinsed for another 2 min. The retention time (T_R) of standard chemicals including DMSO, DMF, methyl acetate, pyridine, phenol and nitrobenzene were acquired, and the standard curve was plotted between their log *P* and log T_R. The HPLC trials of samples were recorded, and their log *P* were then estimated based on their T_R with the aid of the standard curve.

Evaluation of Kinetic Inertness. The kinetic inertness of complexes was examined by using both relaxometric and HPLC methods. **Gd-L$_{1-6}$** were dissolved in 1 M of HCl or KOH to acquire a concentration of 1 mM, and then the complexes were incubated at room temperature and measured using a 1.4 T MR magnet for T_2 relaxation time or a RP-HPLC for decomplexation check. The instrument method of HPLC analysis is according to the description in

HPLC methods. For the transmetallation study, 1 mM of **Gd-L$_{1-6}$** were dissolved in 1×PBS (pH 7.4) containing 10 folds of excess Zn^{2+}, and then 200 μL of the mixture in NMR tube was heated to 80 °C for incubation before measuring T_2 relaxation time. The ratios between T_2 relaxation time after certain time of incubation and its original value ($T_2(t)/T_2(0)$) were plotted *versus* time, which reflected the degree of transmetallation.

Thermodynamic Studies. The pH-potentiometric titrations were conducted on a Metrohm Eco titrator at 25 °C. The ligands were dissolved in 0.1 M of KCl solution, and the pH of the solution was adjusted with 1 M of HCl to be around 1.7, with the total volume fixed at 10 mL and ligands concentration at 2 mM. The titration started with addition of 0.01 mL of KOH solution (0.5 M) for each point under nitrogen atmosphere and ended with the measured pH reached 12.0. The acquired volume-pH data were analyzed using Hyperquad2013 to produce the protonation constants.[56]

An "out of cell" method was adopted for evaluating the stability constants.[25] Each ligand (2.05 mM) and Gd^{3+} (2 mM) were dissolved in 0.1 M of KCl solution with a volume of 2 mL, and around 20 tubes of this solution were titrated with KOH solution (0.1 M) to acquire variations in pH from around pH 1.7 to 8.0. The tubes were then sealed and heated to 60 °C for one week, afterwards the pH of these solutions was measured using a METTLER TOLEDO pH meter at 25 °C. The thermostability constants and pGd values at pH 7.4 were produced from Hyperquad2013 based on the protonation constants of ligand and the acquired volume-pH data.[56] The pH-potentiometric titrations were performed in triplicates and the standard deviations were calculated.

Molecular Docking Studies. AutoDock Suite was adopted for performing protein–ligand docking calculations.[57] The three-dimensional structure of Gd-EOB-DTPA was optimized from the crystal of Gd-DTPA[58] by using Avogadro, and the DFT calculated SAP-S isomer of **Gd-L$_5$** was adopted for simulations. The three-dimensional structures of OATP1B1, OATP1B3, OATP2B1 (PDB code, 2GFP) and NTCP (PDB code, 3ZUY) were referred to previous reports.[16, 48] The docking results with the lowest energy releases were further uploaded to Protein-Ligand Interaction Profiler (PLIP)[59] for analyzing the binding sites and their types of interaction. PyMOL was used to produce the images of GBCAs bound to transporters.

***In vivo* MRI of Normal Mice**. All animal experiments were carried out according to the Institutional Ethical Guidelines on Animal Care and were approved by the Institute of Animal Care and Use Committee at Wenzhou Institute UCAS. Male BALB/c mice (20±3 g, Charles River, China) were used for MRI experiment with a 3.0 T MR scanner (Ingenia elition, Philips) equipped with a custom made mice coil. The mice were firstly anesthetized with Zoletil-50 (80 mg/kg) and xylazine (20 mg/kg), then fixed in the coil for background scan, which was followed by administration of GBCAs *via* tail vein injection (0.1 mmol/kg), with subsequent T_1-weighted images of both coronal and axial planes recorded for around 30 min. The parameters of MRI scanner were set as TE = 9.7 ms, TR = 191.1 ms, FA = 50°, FOV = 50 × 50 mm, matrix size = 200 × 135, 12 slices and slice thickness = 1.5 mm with 0.15 mm interval. Bromosulfophthalein (BSP) was used as the competitor for OATPs, and 50 mM of BSP in PBS (pH 7.4) was injected to the mice *via* tail vein at a dose of 0.1 mmol/kg for 3 times, *i.e.* 45, 30, and 15 min before administration of GBCAs. The MRI experiments were conducted in a triplicate study.

***In vivo* MRI of Mice with Liver Cancer**. The orthotopic HCC model of mice was built from male BALB/c mice (20±3 g, Charles River, China). After acclimation for one week, the mice were fasted 12 hours before operation. Zoletil-50 (80 mg/kg) and xylazine (20 mg/kg) were used for mice anesthesia, and disinfection before surgery was conducted by using iodophor. The pre-grown HuH7 tumor seeds were implanted into the right lobe of the liver through a right abdominal transverse incision, and the incision was sutured properly after sending the liver back to abdominal cavity, with antibiotics applied in next few days for avoiding infection. The mice were allowed to recover in a warmed-up cage and used for MR scanning 2 weeks after inoculation. The MR scanning was conducted following the parameters described above.

Biodistribution Study. BALB/c mice (20±3 g, Charles River, China) were used for the biodistribution study of **Gd-L$_2$** and **Gd-L$_5$**. The mice were euthanized 5 min, 30 min, 24 hours and 48 hours (for **Gd-L$_5$** only) after intravenous injection of complexes (0.1 mmol/kg), and the tissues including brain, heart, liver, spleen, lung, kidney, muscle and intestine were collected for Gd^{3+} analysis. 0.1 g of organs and tissue were weighed and were mixed with 0.2 mL of concentrated nitric acid in centrifuge tubes respectively. After digestion at 70 °C for 12 hours, the mixtures were diluted with 2% nitric acid and filtered, followed by Gd^{3+} quantification using the Agilent 7850 ICP-MS. The experiments were performed in triplicates.

Cytotoxicity Assessments. Human fetal hepatocyte cells LO2 and human embryonic kidney cells 293 (HEK-293) were used for evaluating cytotoxicity of complexes Gd-DOTA and **Gd-L$_{1-8}$**. Both two cell lines were seeded in 96-well plates with 5000 cells per well in 100 μL of Dulbecco's modified Eagle's medium (DMEM), respectively, followed with 24 hours of incubation at 37 °C, 5% CO_2 and saturated humidity. Complexes were dissolved in DMEM to give concentrations at 0.01, 0.05, 0.1, 0.3, 0.5 and 1.0 mM respectively, and the LO2 and HEK-293 cells were rinsed with PBS (pH 7.4) before incubation with complexes in 100 μL of DMEM. After 24 hours under standard condition, the cells were added with 10 μL of cell counting kit-8 (CCK-8) solution, and then incubated for 1 more hour before recording the absorption of samples at 450 nm using a microplate reader. The viability of cells was calculated by comparing to the control group without adding complexes, and the experiment was repeated in triplicates.

***In vivo* Biosafety Evaluation**. Gd-DOTA and **Gd-L$_5$** were applied to male BALB/c mice (20±3 g, Charles River, China) for evaluation of acute and subacute toxicity. The subacute toxicity group (n = 3) was injected with Gd-DOTA or **Gd-L$_5$** (0.1 mmol/kg) in PBS (pH 7.4) *via* tail vein each week for 4 weeks before analysis, while the acute toxicity group (n = 3) was euthanized 24 hours after injection of complexes (0.1 mmol/kg). Blood samples were collected for biomarkers analyses, including alanine aminotransferase (ALT), aspartate aminotransferase (AST) and alkaline phosphatase (ALP), blood urea nitrogen (BUN), creatinine (CR), creati-

nine kinase MB (CK), albumin (ALB), and lactate dehydrogenase (LDH).

Major organs including heart, liver, lung, spleen and kidney were collected for histological analysis. Tissues of organs were fixed in 4% paraformaldehyde, dehydrated, embedded in paraffin, and sectioned. The representative sections were subjected to hematoxylin and eosin (H&E) staining. The images of slides were recorded under a confocal microscope. Each item for analysis was repeated for 3 times, and the results were given as mean ± SD.

***In vivo* MRI of Subcutaneous 4T1 Tumor Mice**. The 4T1 cells were cultured with RPMI1640 medium in six-well cell culture plates and then harvested by centrifugation after treatment with Trypsin-EDTA solution. After removing the supernatant, the cells were resuspended in 1 mL of fresh medium at a concentration of 1×10^7/mL. Then 0.1 mL of this solution was injected to the right side of axillary, and the BALB/c mice were ready for MR scanning when the size of tumor reached around 0.5 cm. A 3.0 T MR scanner (Ingenia elition, Philips) was used for recording T_1-weighted images at representative time points, *e.g.* 5 min, 20 min, 60 min and 120 min postinjection of CAs (0.1 mmol/kg). The parameters of the scanner were set according to previous description, and the experiment was conducted as a triplicate study.

Data Analysis of MRI. MRI images were analyzed using MicroDicom viewer and signal intensity (SI) was read by drawing regions of interest (ROI) on organs/tissues including liver, kidney, tumor and muscle. The uptakes of CAs by liver and kidney were described by relative enhancement (RE), calculated as $(SI_{post} - SI_{pre})/SI_{pre} \times 100\%$, where the SI_{pre} and SI_{post} were signal intensities before and after administration of CAs. The liver to tumor contrast to noise ratio (CNR) was described as $(SI_{liver} - SI_{tumor})/SD_{air}$, in which SD_{air} is the standard deviation (SD) of the signal intensity in the ROI adjacent to the mice. The tumor to muscle CNR (calculated as $(SI_{tumor} - SI_{muscle})/SD_{air}$) was adopted to describe the contrast enhancement of 4T1 subcutaneous tumor after injection of CAs.

***In vitro* Enzymatic Nitroreductase Reaction**. PBS (pH 7.4) was firstly treated in a 1% hypoxia chamber (SCI-tive-Dual chamber hypoxia workstation, Baker Ruskinn) for 24 hours to remove the dissolved oxygen. Afterwards, 10 μl of **Gd-L$_8$** (10 mM), β-Nicotinamide adenine dinucleotide (β-NADH, 100 mM) and recombinant E. coli nitroreductase protein (NTR, 1 μg/μL) were mixed with 1ml of the treated PBS and further incubated for 24 hours under 1% hypoxia condition. 10 μL of NTR was added after 4 and 8 hours of incubation respectively. The reduction of **Gd-L$_8$** was then analyzed using an Agilent 1290 Infinity II UHPLC equipped with an Agilent ZORBAX RRHD Eclipse plus C18 column (1.8μm, 2.1 x 50mm), and the mass spectrometry was acquired using an Agilent 6540 Quadrupole-ToF with an electrospray ionization source in positive ion mode.

ASSOCIATED CONTENT

Supporting Information.

Synthetic procedures, fitting curves for relaxivity determination, analytical HPLC trials for log *P* determination and inertness assessments, additional images of MR scanning, data for biodistributions in mice, HPLC-MS of enzyme catalyzed reduction, and structural characterizations of complexes and their intermediates.

PDB files for DFT calculations and PBD files for molecular docking study.

Molecular formula strings.

This material is available free of charge via the Internet at http://pubs.acs.org.

AUTHOR INFORMATION

Corresponding Authors

Lixiong Dai – *Wenzhou Institute, University of Chinese Academy of Sciences, Wenzhou, Zhejiang, 325000, China; Joint Centre of Translational Medicine, The First Affiliated Hospital of Wenzhou Medical University, Wenzhou, Zhejiang, 325035, China; Zhejiang Engineering Research Center for Innovation and Application of Intelligent Radiotherapy Technology, The Second Affiliated Hospital of Wenzhou Medical University, Wenzhou, Zhejiang, 325000, China; Email: dailx@ucas.ac.cn.*

***Zhihan Yan* –** *Department of Radiology, The Second Affiliated Hospital and Yuying Children's Hospital of Wenzhou Medical University, Wenzhou, Zhejiang, 325027, China. Email: zhihanyan@hotmail.com.*

Fangfu Ye – *Wenzhou Institute, University of Chinese Academy of Sciences, Wenzhou, Zhejiang, 325000, China; Joint Centre of Translational Medicine, The First Affiliated Hospital of Wenzhou Medical University, Wenzhou, Zhejiang, 325035, China; Oujiang Laboratory (Zhejiang Lab for Regenerative Medicine, Vision and Brain Health), Wenzhou, Zhejiang, 325000, China. Email: fye@iphy.ac.cn*.

Yanjuan Gu – *The Hong Kong Polytechnic University Shenzhen Research Institute, Shenzhen, Guangdong, 518057, China. Email: yanjuan.gu@polyu.edu.hk.*

Authors

Weiyuan Xu – *Wenzhou Institute, University of Chinese Academy of Sciences, Wenzhou, Zhejiang, 325000, China; Oujiang Laboratory (Zhejiang Lab for Regenerative Medicine, Vision and Brain Health), Wenzhou, Zhejiang, 325000, China.*

Xinjian Ye – *Department of Radiology, The Second Affiliated Hospital and Yuying Children's Hospital of Wenzhou Medical University, Wenzhou, Zhejiang, 325027, China.*

Min Wu – *Department of Radiology and Huaxi MR Research Center (HMRRC), Functional and Molecular lmaging Key Laboratory of Sichuan Province, West China Hospital, Sichuan University, Chengdu, Sichuan, 610041, China.*

Xin Jiang – *Wenzhou Institute, University of Chinese Academy of Sciences, Wenzhou, Zhejiang, 325000, China.*

Lik Hang Hugo TSE – *The Hong Kong Polytechnic University Shenzhen Research Institute, Shenzhen, Guangdong, 518057, China.*

Kun Shu – *Department of Radiology, The Second Affiliated Hospital and Yuying Children's Hospital of Wenzhou Medical University, Wenzhou, Zhejiang, 325027, China.*

Liuhui Xu – *Joint Centre of Translational Medicine, The First Affiliated Hospital of Wenzhou Medical University, Wenzhou, Zhejiang, 325035, China.*

Yong Jian – *Wenzhou Institute, University of Chinese Academy of Sciences, Wenzhou, Zhejiang, 325000, China.*

Gengshen Mo – *Wenzhou Institute, University of Chinese Academy of Sciences, Wenzhou, Zhejiang, 325000, China.*

Jiao Xu – *Wenzhou Institute, University of Chinese Academy of Sciences, Wenzhou, Zhejiang, 325000, China*.

Yinghui Ding – *Wenzhou Institute, University of Chinese Academy of Sciences, Wenzhou, Zhejiang, 325000, China.*

Ruonan Gao – *Wenzhou Institute, University of Chinese Academy of Sciences, Wenzhou, Zhejiang, 325000, China.*
Jianliang Shen – *Wenzhou Institute, University of Chinese Academy of Sciences, Wenzhou, Zhejiang, 325000, China.*

Author Contributions

‡W.X., X.Y. and M.W. contributed equally. All authors have given approval to the final version of the manuscript.

Notes

The authors declare no competing interests.

ACKNOWLEDGMENT

This work was financially supported by the National Natural Science Foundation of China (22075281, 32071376, 22105201), Zhenjiang Provincial Natural Science of Foundation of China (LZ21B010001), University of Chinese Academy of Science (WIUCASQD2020008); Wenzhou Fund of Science and Technology (2021Y0163); and Anhui Laboratory of Molecule-Based Materials (Fzj21002). Dr. Huaping Li from Wenzhou Institute, UCAS and Dr. Jiaxi Ru from Wenzhou Medical University are acknowledged for their help in molecular docking study and data treatment.

ABBREVIATIONS

ACN, acetonitrile; AIBN, azodiisobutyronitrile; BSP, bromosulfophthalein; CAs, contrast agents; CNR, contrast to noise ratio, DOTA, 1,4,7,10-tetraazacyclododecane-1,4,7,10-tetraacetic acid; EOB, ethoxybenzyl; GBCAs, Gd^{3+}-based contrast agents; HCC, hepatocellular carcinoma; HEK-293, human embryonic kidney cells 293; HuH7, human hepatoma 7; MRI, magnetic resonance imaging; MS, mass spectrometry; NBS, N-bromosuccinimide; NMR, nuclear magnetic resonance; NSF, nephrogenic systemic fibrosis; NTCP, Na^{+}-dependent taurocholate transporting polypeptide; OATPs, organic anion transporting polypeptides; PBS, phosphate buffered saline; RP-HPLC, reverse phase high performance liquid chromatography; SAP, square antiprismatic; TSAP, twisted square antiprismatic.

REFERENCES

1. Lohrke, J.; Frenzel, T.; Endrikat, J.; Alves, F. C.; Grist, T. M.; Law, M.; Lee, J. M.; Leiner, T.; Li, K. C.; Nikolaou, K.; Prince, M. R.; Schild, H. H.; Weinreb, J. C.; Yoshikawa, K.; Pietsch, H., 25 Years of Contrast-Enhanced MRI: Developments, Current Challenges and Future Perspectives. *Adv. Ther.* **2016,** *33* (1), 1-28.
2. Caravan, P.; Ellison, J. J.; McMurry, T. J.; Lauffer, R. B., Gadolinium(III) Chelates as MRI Contrast Agents: Structure, Dynamics, and Applications. *Chem. Rev.* **1999,** *99* (9), 2293-2352.
3. Marckmann, P.; Skov, L.; Rossen, K.; Dupont, A.; Damholt, M. B.; Heaf, J. G.; Thomsen, H. S., Nephrogenic Systemic Fibrosis: Suspected Causative Role of Gadodiamide used for Contrast-enhanced Magnetic Resonance Imaging. *J. Am. Soc. Nephrol.* **2006,** *17* (9), 2359-2362.
4. Grobner, T., Gadolinium - A Specific Trigger for the Development of Nephrogenic Fibrosing Dermopathy and Nephrogenic Systemic Fibrosis? *Nephrol. Dial. Transplant* **2006,** *21* (4), 1104-1108.
5. Yang, L.; Krefting, I.; Gorovets, A.; Marzella, L.; Kaiser, J.; Boucher, R.; Rieves, D., Nephrogenic Systemic Fibrosis and Class Labeling of Gadolinium-based Contrast Agents by the Food and Drug Administration. *Radiology* **2012,** *265* (1), 248-253.
6. Kanda, T.; Osawa, M.; Oba, H.; Toyoda, K.; Kotoku, J.; Haruyama, T.; Takeshita, K.; Furui, S., High Signal Intensity in Dentate Nucleus on Unenhanced T1-weighted MR Images: Association with Linear versus Macrocyclic Gadolinium Chelate Administration. *Radiology* **2015,** *275* (3), 803-809.
7. Zhang, Y.; Cao, Y.; Shih, G. L.; Hecht, E. M.; Prince, M. R., Extent of Signal Hyperintensity on Unenhanced T1-weighted Brain MR Images after More than 35 Administrations of Linear Gadolinium-based Contrast Agents. *Radiology* **2017,** *282* (2), 516-525.
8. Wahsner, J.; Gale, E. M.; Rodriguez-Rodriguez, A.; Caravan, P., Chemistry of MRI Contrast Agents: Current Challenges and New Frontiers. *Chem. Rev.* **2019,** *119* (2), 957-1057.
9. Di Bari, L.; Salvadori, P., Static and Dynamic Stereochemistry of Chiral Ln DOTA Analogues. *Chemphyschem* **2011,** *12* (8), 1490-1497.
10. Dai, L.; Jones, C. M.; Chan, W. T. K.; Pham, T. A.; Ling, X.; Gale, E. M.; Rotile, N. J.; Tai, W. C.; Anderson, C. J.; Caravan, P.; Law, G. L., Chiral DOTA Chelators as an Improved Platform for Biomedical Imaging and Therapy Applications. *Nat. Commun.* **2018,** *9* (1), 857.
11. Clough, T. J.; Jiang, L.; Wong, K. L.; Long, N. J., Ligand Design Strategies to Increase Stability of Gadolinium-based Magnetic Resonance Imaging Contrast Agents. *Nat. Commun.* **2019,** *10* (1), 1420.
12. Payne, K. M.; Woods, M., Isomerism in Benzyl-DOTA Derived Bifunctional Chelators: Implications for Molecular Imaging. *Bioconjugate Chem.* **2015,** *26* (2), 338-344.
13. Dai, L.; Lo, W. S.; Coates, I. D.; Pal, R.; Law, G. L., New Class of Bright and Highly Stable Chiral Cyclen Europium Complexes for Circularly Polarized Luminescence Applications. *Inorg. Chem.* **2016,** *55* (17), 9065-9070.
14. Dai, L.; Zhang, J.; Chen, Y.; Mackenzie, L. E.; Pal, R.; Law, G. L., Synthesis of Water-Soluble Chiral DOTA Lanthanide Complexes with Predominantly Twisted Square Antiprism Isomers and Circularly Polarized Luminescence. *Inorg. Chem.* **2019,** *58* (19), 12506-12510.
15. Zhang, J.; Dai, L.; Webster, A. M.; Chan, W. T. K.; Mackenzie, L. E.; Pal, R.; Cobb, S. L.; Law, G. L., Unusual Magnetic Field Responsive Circularly Polarized Luminescence Probes with Highly Emissive Chiral Europium(III) Complexes. *Angew. Chem. Int. Ed.* **2021,** *60* (2), 1004-1010.
16. Baek, A. R.; Kim, H. K.; Kim, S.; Yang, J. U.; Kang, M. K.; Lee, J. J.; Sung, B.; Lee, H.; Kim, M.; Cho, A. E.; Park, J. A.; Chang, Y., Effect of Structural Fine-Tuning on Chelate Stability and Liver Uptake of Anionic MRI Contrast Agents. *J. Med. Chem.* **2022,** *65* (8), 6313-6324.
17. Baek, A. R.; Kim, H. K.; Park, S.; Lee, G. H.; Kang, H. J.; Jung, J. C.; Park, J. S.; Ryeom, H. K.; Kim, T. J.; Chang, Y., Gadolinium Complex of 1,4,7,10-Tetraazacyclododecane-1,4,7-trisacetic Acid (DO3A)-Ethoxybenzyl (EOB) Conjugate as a New Macrocyclic Hepatobiliary MRI Contrast Agent. *J. Med. Chem.* **2017,** *60* (12), 4861-4868.
18. Hall, R. C.; Qin, J.; Laney, V.; Ayat, N.; Lu, Z. R., Manganese(II) EOB-Pyclen Diacetate for Liver-Specific MRI. *ACS Appl. Bio. Mater.* **2022,** *5* (2), 451-458.
19. Zhang, H.; Guo, Y.; Jiao, J.; Qiu, Y.; Miao, Y.; He, Y.; Li, Z.; Xia, C.; Li, L.; Cai, J.; Xu, K.; Liu, X.; Zhang, C.; Bay, B. H.; Song, S.; Yang, Y.; Peng, M.; Wang, Y.; Fan, H., A Hepatocyte-targeting Nanoparticle for Enhanced Hepatobiliary Magnetic Resonance Imaging. *Nat. Biomed. Eng.* **2022,** *7*, 221-235.
20. Lu, Z. R.; Laney, V.; Li, Y., Targeted Contrast Agents for Magnetic Resonance Molecular Imaging of Cancer. *Acc. Chem. Res.* **2022,** *55* (19), 2833-2847.
21. Li, Y.; Gao, S.; Jiang, H.; Ayat, N.; Laney, V.; Nicolescu, C.; Sun, W.; Tweedle, M. F.; Lu, Z. R., Evaluation of Physicochemical Properties, Pharmacokinetics, Biodistribution, Toxicity, and Contrast-Enhanced Cancer MRI of a Cancer-Targeting Contrast Agent, MT218. *Invest. Radiol.* **2022,** *57* (10), 639-654.
22. Vaidya, A.; Ayat, N.; Buford, M.; Wang, H.; Shankardass, A.; Zhao, Y.; Gilmore, H.; Wang, Z.; Lu, Z. R., Noninvasive Assessment and Therapeutic Monitoring of Drug-resistant Colorectal Cancer by MR Molecular Imaging of Extradomain-B Fibronectin. *Theranostics* **2020,** *10* (24), 11127-11143.
23. Zhang, R. R.; Choi, C.; Brunnquell, C. L.; Hernandez, R.; Pinchuk, A. N.; Grudzinski, J. G.; Clark, P. A.; McMillan, A. B.; Audhya, A.; Jeffrey, J.; Kuo, J. S.; Weichert, J. P., Next-Generation Cancer Magnetic Resonance Imaging With Tumor-Targeted Alkylphosphocholine Metal Analogs. *Invest. Radiol.* **2022,** *57* (10), 655-663.
24. Xu, W.; Lu, Y.; Xu, J.; Li, H.; Lan, R.; Gao, R.; Ding, Y.; Ye, X.; Shu, K.; Ye, F.; Yan, Z.; Dai, L., Rational Design of Gd-DOTA-Type Contrast Agents for Hepatobiliary Magnetic Resonance Imaging. *J. Med. Chem.* **2023,** *66* (13), 8993-9005.
25. Aime, S.; Botta, M.; Garda, Z.; Kucera, B. E.; Tircso, G.; Young, V. G.; Woods, M., Properties, Solution State Behavior, and

Crystal Structures of Chelates of DOTMA. *Inorg. Chem.* **2011,** *50* (17), 7955-7965.
26. Karan, S.; Cho, M. Y.; Lee, H.; Park, H. S.; Han, E. H.; Song, Y.; Lee, Y.; Kim, M.; Cho, J. H.; Sessler, J. L.; Hong, K. S., Hypoxia-Responsive Luminescent CEST MRI Agent for In Vitro and In Vivo Tumor Detection and Imaging. *J. Med. Chem.* **2022,** *65* (10), 7106-7117.
27. O'Connor, J. P. B.; Robinson, S. P.; Waterton, J. C., Imaging Tumour Hypoxia with Oxygen-enhanced MRI and BOLD MRI. *Br. J. Radiol.* **2019,** *92* (1095), 20180642.
28. Liu, J. N.; Bu, W.; Shi, J., Chemical Design and Synthesis of Functionalized Probes for Imaging and Treating Tumor Hypoxia. *Chem. Rev.* **2017,** *117* (9), 6160-6224.
29. Han, Y.; Zhou, X.; Qian, Y.; Hu, H.; Zhou, Z.; Liu, X.; Tang, J.; Shen, Y., Hypoxia-targeting Dendritic MRI Contrast Agent Based on Internally Hydroxy Dendrimer for Tumor Imaging. *Biomaterials* **2019,** *213*, 119195.
30. Iikuni, S.; Ono, M.; Watanabe, H.; Shimizu, Y.; Sano, K.; Saji, H., Cancer Radiotheranostics Targeting Carbonic Anhydrase-IX with (111)In- and (90)Y-labeled Ureidosulfonamide Scaffold for SPECT Imaging and Radionuclide-based Therapy. *Theranostics* **2018,** *8* (11), 2992-3006.
31. Cao, W.; Yang, J.; Zhu, C.; Zeng, Z.; Yang, C.; Chen, T.; Zhu, J., Carbonic Anhydrase IX Targeting Mn(II)-Based Magnetic Resonance Molecular Imaging Probe for Hypoxia Tumors. *Bioconjugate Chem.* **2023,** *34* (6), 1166-1175.
32. Nocentini, A.; Trallori, E.; Singh, S.; Lomelino, C. L.; Bartolucci, G.; Di Cesare Mannelli, L.; Ghelardini, C.; McKenna, R.; Gratteri, P.; Supuran, C. T., 4-Hydroxy-3-nitro-5-ureido-benzenesulfonamides Selectively Target the Tumor-Associated Carbonic Anhydrase Isoforms IX and XII Showing Hypoxia-Enhanced Antiproliferative Profiles. *J. Med. Chem.* **2018,** *61* (23), 10860-10874.
33. D'Ambrosio, K.; Vitale, R. M.; Dogné, J. M.; Masereel, B.; Innocenti, A.; Scozzafava, A.; De Simone, G.; Supuran, C. T., Carbonic Anhydrase Inhibitors: Bioreductive Nitro-containing Sulfonamides with Selectivity for Targeting the Tumor Associated Isoforms IX and XII. *J. Med. Chem.* **2008,** *51* (11), 3230-3237.
34. Szablewski, L., Expression of Glucose Transporters in Cancers. *Biochim. Biophys. Acta* **2013,** *1835* (2), 164-169.
35. Caravan, P.; Cloutier, N. J.; Greenfield, M. T.; McDermid, S. A.; Dunham, S. U.; Bulte, J. W.; Amedio, J. C., Jr.; Looby, R. J.; Supkowski, R. M.; Horrocks, W. D., Jr.; McMurry, T. J.; Lauffer, R. B., The Interaction of MS-325 with Human Serum Albumin and Its Effect on Proton Relaxation Rates. *J. Am. Chem. Soc.* **2002,** *124* (12), 3152-3162.
36. Wang, J.; Wang, H.; Ramsay, I. A.; Erstad, D. J.; Fuchs, B. C.; Tanabe, K. K.; Caravan, P.; Gale, E. M., Manganese-Based Contrast Agents for Magnetic Resonance Imaging of Liver Tumors: Structure-Activity Relationships and Lead Candidate Evaluation. *J. Med. Chem.* **2018,** *61* (19), 8811-8824.
37. Chen, K.; Li, P.; Zhu, C.; Xia, Z.; Xia, Q.; Zhong, L.; Xiao, B.; Cheng, T.; Wu, C.; Shen, C.; Zhang, X.; Zhu, J., Mn(II) Complex of Lipophilic Group-Modified Ethylenediaminetetraacetic Acid (EDTA) as a New Hepatobiliary MRI Contrast Agent. *J. Med. Chem.* **2021,** *64* (13), 9182-9192.
38. Port, M.; Idee, J. M.; Medina, C.; Robic, C.; Sabatou, M.; Corot, C., Efficiency, thermodynamic and kinetic stability of marketed gadolinium chelates and their possible clinical consequences: a critical review. *Biometals* **2008,** *21* (4), 469-490.
39. Dai, L.; Zhang, J.; Wong, C. T.; Chan, W. T. K.; Ling, X.; Anderson, C. J.; Law, G. L., Design of Functional Chiral Cyclen-Based Radiometal Chelators for Theranostics. *Inorg. Chem.* **2021,** *60* (10), 7082-7088.
40. Kalman, F. K.; Woods, M.; Caravan, P.; Jurek, P.; Spiller, M.; Tircso, G.; Kiraly, R.; Brucher, E.; Sherry, A. D., Potentiometric and Relaxometric Properties of A Gadolinium-based MRI Contrast Agent for Sensing Tissue pH. *Inorg. Chem.* **2007,** *46* (13), 5260-5270.
41. Burai, L.; Fábián, I.; Király, R.; Szilágyi, E.; Brücher, E., Equilibrium and Kinetic Studies on the Formation of the Lanthanide(III) cComplexes, [Ce(dota)]− and [Yb(dota)]− (H4dota = 1,4,7,10-tetraazacyclododecane-1,4,7,10-tetraacetic acid). *J. Chem. Soc., Dalton T.* **1998,** (2), 243-248.
42. Cacheris, W. P.; Nickle, S. K.; Sherry, A. D., Thermodynamic Study of Lanthanide Complexes of 1,4,7-Triazacyclononane-N,N',N"-triacetic Acid and 1,4,7,10-Tetraazacyclododecane-N,N',N",N"'-tetraacetic Acid. *Inorg. Chem.* **1987,** *26* (6), 958-960.
43. Tircso, G.; Webber, B. C.; Kucera, B. E.; Young, V. G.; Woods, M., Analysis of the Conformational Behavior and Stability of the SAP and TSAP Isomers of Lanthanide(III) NB-DOTA-type Chelates. *Inorg. Chem.* **2011,** *50* (17), 7966-7979.
44. Haimerl, M.; Utpatel, K.; Götz, A.; Zeman, F.; Fellner, C.; Nickel, D.; Luerken, L.; Brennfleck, F. W.; Stroszczynski, C.; Scheiter, A.; Verloh, N., Quantification of Contrast Agent Uptake in the Hepatobiliary Phase Helps to Differentiate Hepatocellular Carcinoma Grade. *Sci. Rep.* **2021,** *11,* 22991.
45. Jouan, E.; Le Vée, M.; Denizot, C.; Parmentier, Y.; Fardel, O., Drug Transporter Expression and Activity in Human Hepatoma HuH-7 Cells. *Pharmaceutics* **2016,** *9* (1), 3.
46. Zhao, Z.; Zhen, M.; Zhou, C.; Li, L.; Jia, W.; Liu, S.; Li, X.; Liao, X.; Wang, C., A Gadofullerene Based Liver-specific MRI Contrast Agent for an Early Diagnosis of Orthotopic Hepatocellular Carcinoma. *J. Mater. Chem. B* **2021,** *9* (28), 5722-5728.
47. Taniguchi, T.; Zanetti-Yabur, A.; Wang, P.; Usyk, M.; Burk, R. D.; Wolkoff, A. W., Interindividual Diversity in Expression of Organic Anion Uptake Transporters in Normal and Cirrhotic Human Liver. *Hepatol. Commun.* **2020,** *4* (5), 739-752.
48. Islam, M. K.; Kim, S.; Kim, H. K.; Kim, Y. H.; Lee, Y. M.; Choi, G.; Baek, A. R.; Sung, B. K.; Kim, M.; Cho, A. E.; Kang, H.; Lee, G. H.; Choi, S. H.; Lee, T.; Park, J. A.; Chang, Y., Synthesis and Evaluation of Manganese(II)-Based Ethylenediaminetetraacetic Acid-Ethoxybenzyl Conjugate as a Highly Stable Hepatobiliary Magnetic Resonance Imaging Contrast Agent. *Bioconjug. Chem.* **2018,** *29* (11), 3614-3625.
49. Frydrychowicz, A.; Lubner, M. G.; Brown, J. J.; Merkle, E. M.; Nagle, S. K.; Rofsky, N. M.; Reeder, S. B., Hepatobiliary MR Imaging with Gadolinium-based Contrast Agents. *J. Magn. Reson. Imaging* **2012,** *35* (3), 492-511.
50. Zhang, Q.; Zhou, D.; Fang, G.; Lu, H.; Zeng, J.; Gu, Z., Cell‐Derived Biomimetic 2D Nanoparticles to Improve Cell‐Specific Targeting and Tissue Penetration for Enhanced Magnetic Resonance Imaging. *Adv. Mater. Interfaces* **2022,** *9* (7), 2101914.
51. Liberti, M. V.; Locasale, J. W., The Warburg Effect: How Does it Benefit Cancer Cells? *Trends Biochem. Sci.* **2016,** *41* (3), 211-218.
52. Aghighi, M.; Golovko, D.; Ansari, C.; Marina, N. M.; Pisani, L.; Kurlander, L.; Klenk, C.; Bhaumik, S.; Wendland, M.; Daldrup-Link, H. E., Imaging Tumor Necrosis with Ferumoxytol. *PLoS One* **2015,** *10* (11), e0142665.
53. Purkerson, J. M.; Schwartz, G. J., The Role of Carbonic Anhydrases in Renal Physiology. *Kidney Int.* **2007,** *71* (2), 103-115.
54. Frisch M. J.; Trucks, G. W. S., H. B.; Scuseria, G. E.; Robb, M. A.; Cheeseman, J. R.; Scalmani, G.; Barone V.; Mennucci, B.; Petersson, G. A.; Nakatsuji, H.; Caricato, M.; Li X.; Hratchian, H. P.; Izmaylov. A. F.; Bloino J.; Zheng, G.; Sonnenberg, J. L.; Hada, M.; Ehara, M.; Toyota, K.; Fukuda, R.; Hasegawa, J.; Ishida M.; Nakajima T.; Honda, Y.; Kitao, O.; Nakai, H.; Vreven, T.; Mont-gomery J. A.; Jr.; Peralta, J. E.; Ogliaro, F.; Bearpark, M.; Heyd, J. J.; Brothers, E.; Kudin, K. N.; Staroverov, V. N.; Keith T.; Koba-yashi, R.; Normand, J.; Raghavachari, K.; Rendell, A.; Burant, J. C.; Iyengar, S. S.; Tomasi, J.; Cossi, M.; Rega, N.; Millam, J. M.; Klene, M.; Knox, J. E.; Cross, J. B.; Bakken, V.; Adamo, C.; Jara-millo, J.; Gomperts, R.; Stratmann, R. E.; Yazyev, O.; Austin, A. J.; Cammi, R.; Pomelli, C.; Ochterski, J. W.; Martin, R. L.; Morokuma, K.; Zakrzewski, V. G.; Voth, G. A.; Salvador, P.; Dan-nenberg, J. J.; Dapprich, S.; Daniels, A. D.; Farkas, O.; Foresman, J. B.; Ortiz, J. V.; Cioslowski, J. and Fox, D. J., Gaussian, Inc., Wallingford CT. **2013**.
55. Chen, X.; Chen, T. T.; Li, W. L.; Lu, J. B.; Zhao, L. J.; Jian, T.; Hu, H. S.; Wang, L. S.; Li, J., Lanthanides with Unusually Low Oxidation States in the PrB_3^- and PrB_4^- Boride Clusters. *Inorg. Chem.* **2019,** *58* (1), 411-418.
56. Gale, E. M.; Atanasova, I. P.; Blasi, F.; Ay, I.; Caravan, P., A Manganese Alternative to Gadolinium for MRI Contrast. *J. Am. Chem. Soc.* **2015,** *137* (49), 15548-15557.
57. Forli, S.; Huey, R.; Pique, M. E.; Sanner, M. F.; Goodsell, D. S.; Olson, A. J., Computational Protein-ligand Docking and Virtual Drug Screening with the AutoDock Suite. *Nat. Protoc.* **2016,** *11* (5), 905-919.
58. Gao, S.; George, S. J.; Zhou, Z.-H., Interaction of Gd-DTPA with Phosphate and Phosphite: Toward the Reaction Intermediate in Nephrogenic Systemic Fibrosis. *Dalton T.* **2016,** *45* (12), 5388-5394.

59. Adasme, M. F.; Linnemann, K. L.; Bolz, S. N.; Kaiser, F.; Salentin, S.; Haupt, V. J.; Schroeder, M., PLIP 2021: Expanding the Scope of the Protein-ligand Interaction Profiler to DNA and RNA. *Nucleic Acids Res.* **2021,** *49* (1), 530-534.

TOC graph

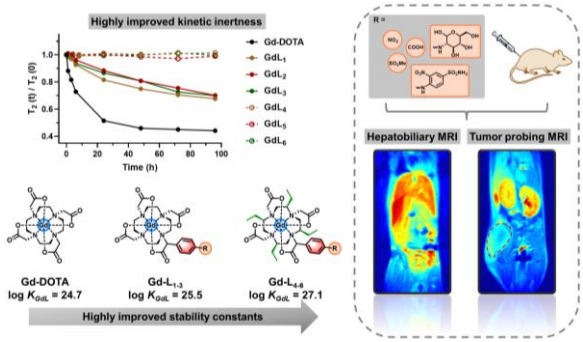
Highly improved kinetic inertness
Gd-DOTA
GdL1
GdL2
GdL3
GdL4
GdL5
GdL6
Time (h)
Gd-DOTA
log KGdL = 24.7
Gd-L1-3
log KGdL = 25.5
Gd-L4-6
log KGdL = 27.1
Highly improved stability constants
R =
Hepatobiliary MRI
Tumor probing MRI